Nonperturbative renormalization with interpolating momentum schemes

N. Garron[1,2] C. Cahill,[2] M. Gorbahn,[2] J. A. Gracey[2] and P. E. L. Rakow[2]

[1]*School of Mathematics, Computer Science and Engineering, Liverpool Hope University,*
Hope Park, Liverpool L16 9JD, United Kingdom
[2]*Theoretical Physics Division, Department of Mathematical Sciences, University of Liverpool,*
Liverpool L69 3BX, United Kingdom

Hadronic matrix elements evaluated on the lattice can be converted to a continuum scheme such as $\overline{\text{MS}}$ using intermediate nonperturbative renormalization schemes. Discretization effects on the lattice and convergence of the continuum perturbation theory are both scheme dependent and we explore this dependence in the framework of the Rome-Southampton method for generalized kinematics. In particular, we implement several nonexceptional *interpolating* momentum schemes, where the momentum transfer is *not* restricted to the symmetric point defined in RI/SMOM. Using flavor nonsinglet quark bilinears, we compute the renormalization factors of the quark mass and wave function for $N_f = 3$ flavors of dynamical quarks. We investigate the perturbative and nonperturbative scale dependencies. Our numerical results are obtained from lattice simulations performed with domain-wall fermions, based on ensembles generated by RBC-UKQCD collaborations; we use two different lattice spacings $1/a \sim 1.79$ and 2.38 GeV. We also give the numerical values for the relevant anomalous dimensions and matching coefficients at next-to-next-to-leading order.

I. INTRODUCTION

One major goal of lattice QCD is to determine the matrix elements of hadronic operators, with particular emphasis on flavor nonsinglet quark bilinear operators, such as the local scalar, vector, axial vector, or pseudoscalar operators. To produce physically meaningful results we need renormalization factors to relate the bare lattice results to quantities in standard renormalization schemes, such as the modified minimal subtraction scheme, $\overline{\text{MS}}$. This conversion can be done in lattice perturbation theory but it is well known that it results in large systematic error because the perturbative series converges poorly. Instead, in the last couple of decades, more efficient methods have been developed, the most popular ones being the Schrödinger functional [1,2] and Rome-Southampton [3] frameworks. In this work we follow the latter. In both cases, the strategy comprises two distinct steps: First the renormalization factors are obtained nonperturbatively from lattice simulations in a given intermediate scheme, hence the name nonperturbative renormalization (NPR). Then these factors are converted to $\overline{\text{MS}}$ providing us with a bridge between low and high energies. This second step is done perturbatively, but in the framework of the Rome-Southampton method, it can be done in standard continuum perturbation theory so that we can take advantage of the multiloop computation available in the literature. In principle the method is relatively simple: one makes lattice measurements of Green's functions with bilinear operators inserted into quark 2-point functions (for example), and compares the lattice results with continuum perturbative results. This method can also be applied to more complicated Green's functions, higher twist bilinears, four-quark operators, etc. It is worth noting that although traditionally we work in a massless limit, a massive momentum scheme has been developed in [4].

In early lattice studies the operator insertion was at zero momentum transfer, see for example [3,5] for the early direction of this approach. This choice of kinematics corresponds to an exceptional momentum configuration and is subject to potential infrared issues. The origin of the problem and potential solutions were already discussed in detail in [6]. These infrared problems can become even more severe when the chiral limit is taken, and had lead to significant discrepancies in the case of neutral meson mixing [7,8]. With the improvement in lattice analyses as well as the use of dynamical fermions, the refinement of the nonperturbative structure that is of phenomenological interest became suspect due to the emergence of the latent infrared issues.

Therefore in [9–12], an extension to the zero momentum insertion for this class of Green's functions was developed. In particular the Green's functions were computed with a nonzero momentum flowing through the operator and external quark legs at what is now termed *the fully symmetric momentum subtraction point* or SMOM.[1] This circumvents any potential ambiguity in assessing infrared effects due to exceptional momentum configurations and in particular in the chiral limit extrapolation. In either scenario of zero or nonzero operator momentum flow lattice measurements were assisted by matching to the continuum limit. By this we mean that one can compute the same Green's function for any of the above operators in the continuum field theory at several loop orders in the $\overline{\text{MS}}$ scheme. For the quark mass, in the zero momentum case this has been carried out to three loops, but for the nonzero momentum case this has only been carried out to two loops, [9–11] though there has been progress towards the next loop order in [13,14]. Such continuum matching allows one to accurately tune to the ultraviolet before extrapolating to the nonperturbative or low energy region where measurements are made and errors estimated.

The effect of using a momentum configuration which is infrared secure can be seen for example in [8,15–19] where the renormalization factors for the various flavor nonsinglet quark bilinear or four-quark operators were calculated for both momentum configurations. A quantity which can be used as a benchmark is the ratio of the vector and axial vector operators. On symmetry grounds this has to be unity for domain-wall fermions and thus provides a stringent test of determining which momentum configuration was more reliable. Similarly, the scalar and pseudoscalar densities should be equal, up to low-energy effects due to spontaneous chiral symmetry breaking. The size of these unwanted contaminations depend on the momentum configuration. It is evident from the analysis of, for example, [15,18,19], that the SMOM ratio Z_A/Z_V is unity over virtually the full momentum range and well into the deep infrared in marked contrast to the zero momentum case. While this augurs well for significant improvement in lattice measurements and errors, one question naturally arises which will form the main focus of our article.

Now that it is established that the SMOM nonexceptional momentum configuration gives a clear improvement, it is only one of many possible configurations that can be studied. Indeed, for example in [9,10], a more general off-shell case was developed which is termed IMOM to denote the interpolating momentum subtraction configuration. In the SMOM definition the momentum squared of the three external momenta were all equal. By contrast in the IMOM case the magnitude of the operator momentum flow is allowed to vary and this is governed by an additional kinematic parameter ω. For example the SMOM case corresponds to $\omega = 1$. Varying ω between 0 and 4, which are the respective values giving infrared or collinear singularities, allows one to search for a value which can improve the matching to the continuum, the nonperturbative behaviour or maybe even reduce the lattice artifacts. This therefore leads to our investigation to see if there is an optimal value for ω, possibly different from one, which minimizes errors and improves benchmarks such as that studied in [15,18,19]. This would be the appropriate next stage after the success of the SMOM schemes. For instance the deviation between the scalar and pseudoscalar operators renormalization factors can be examined to gauge pion mass effects. While ω will be our main parameter the overall momentum scale μ at which measurements are made will also be important. Therefore to have a thorough investigation we have performed a lattice computation of various operators on different lattices for half integer values of ω between 0 and 4 for various values of μ. This has allowed us to identify an optimal area of the (ω, μ^2)-plane where there is an effective plateau upon which measurements are reliably accurate. Moreover the picture appears to be consistent for the operators we consider, though the actual locations are not necessarily the same point for each case. It suggests that there should be a similar qualitative behavior for operators with covariant derivatives or four-quark operators, which we do not consider here.

Although the article primarily concentrates on the lattice computations and analysis, we were indebted throughout to the various two-loop $\overline{\text{MS}}$ continuum results accumulated over the last decade, [9–12,18,20], to facilitate the continuum matching. Moreover the measurement of quark bilinear currents in the IMOM configuration will give crucial directions to 4-point quark Green's functions such as those relevant to kaon mixing for example, [7,8]. In that scenario the effective 4-point functions can be mimicked by products of the Green's functions we consider here. It is particularly important in this case, as it has been argued that the choice of kinematics was responsible for the discrepancy observed in the literature.

The paper is organized as follows: In Sec. II we outline the kinematics setup, explaining in detail how our incoming and outgoing momenta are chosen to lead to a given value of ω for a given value of μ. In Sec. III we explain how we define the Z factors, and discuss our choice of projectors. In Sec. IV, we present our results for the Z factors and their scale evolutions. We conclude in Sec. V. Appendix A shows the perturbative conversion factors for matching from IMOM to $\overline{\text{MS}}$. More details about the lattice simulations can be found in Appendix B. We show the chiral extrapolations in Appendix C. In Appendix D, we collect the results for Z_m for the $\not{q}$ projector. An extensive study of the scale analysis dependence is presented in Appendix E. Finally we show our continuum extrapolations in Appendix F.
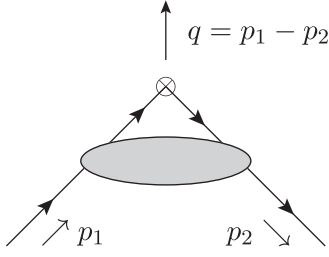
---

[1]To ease the notation we drop the "RI" in RI/SMOM.

FIG. 1. We consider an incoming momentum p_1, outgoing momentum p_2, and a momentum transfer $q = p_1 - p_2$.

II. KINEMATICS

We consider the interaction in Fig. 1, where the incoming momentum is defined as p_1, the outgoing momentum as p_2, and the momentum transfer as q.

The method is based on the Rome-Southampton regularization independent momentum scheme: the fermions are off-shell, we work in the chiral limit, and the renormalization scale is given by the choice of external momenta. In the original RI/MOM scheme (or RI′/MOM) [3], the incoming and outgoing momenta are equal, $p_1 = p_2$, so that there is no momentum transfer, $q = 0$. The renormalization scale μ is defined by $\mu^2 = p_1^2 = p_2^2$. In contrast, in the SMOM schemes, the incoming and outgoing momenta are different: they are chosen such that $q^2 = p_1^2 = p_2^2$; naturally the renormalization scale is given by $\mu = \sqrt{q^2}$. The advantage is to avoid exceptional kinematics which behave badly in the infrared regime [9].

The above schemes can be generalized further. We retain the condition $p_1^2 = p_2^2 = \mu^2$ but drop the requirement $q^2 = \mu^2$. We define the variable $\omega = q^2/\mu^2$ to parametrize the kinematics. $\omega = 0$ corresponds to the original RI/MOM and RI′/MOM schemes, $\omega = 1$ corresponds to the SMOM scheme. The possible values of ω range between 0 and 4. Let us denote by α the angle between the incoming and outgoing momenta. We choose our frame such that the momenta take the following form (the time component is represented by the last entry):

$$p_1 = \mu[1, 0, 0, 0], \tag{2.1}$$

$$p_2 = \mu[\cos\alpha, \sin\alpha, 0, 0]. \tag{2.2}$$

This gives

$$q = p_1 - p_2 = \mu[1 - \cos\alpha, -\sin\alpha, 0, 0], \tag{2.3}$$

and

$$q^2 = \mu^2((1 - \cos\alpha)^2 + \sin^2\alpha)) \tag{2.4}$$

$$= 2\mu^2(1 - \cos\alpha) \tag{2.5}$$
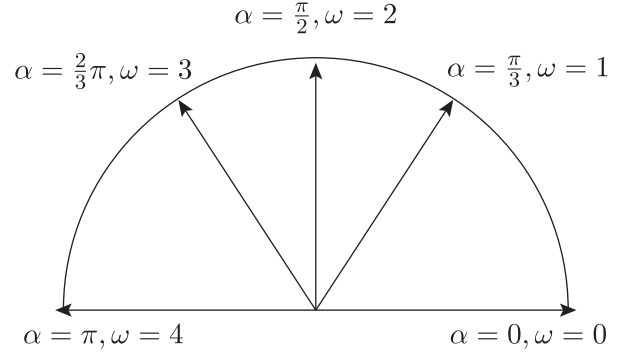
$$\equiv \omega\mu^2, \tag{2.6}$$

FIG. 2. The parameter ω is dependent upon the value of the angle α between the incoming and outgoing momenta.

where we have defined $\omega = 2(1 - \cos\alpha)$. Clearly the parameter ω can take any real value between 0 and 4, and the value of ω is directly related to the value of α as shown in Fig 2.

We can check that the extreme cases $\omega = 0$ and $\omega = 4$ correspond to $p_1 = p_2$ and $p_1 = -p_2$, respectively, and therefore these situations suffer from infrared and collinear singularities. We also note that $\omega = 0$ is the choice made in the original (exceptional) kinematics of a standard RI/MOM scheme while $\omega = 1$ corresponds to the SMOM kinematic of [9]. This has been known for a while, see for example [9,10]. Different choices of ω are referred to as *interpolating momentum* schemes [11,20,21]. However, to our knowledge, there is no numerical study or practical implementation of such kinematics.

Let us now turn to the lattice implementation. If L is the physical spatial extent of the lattice (we do not consider the temporal extent here for simplicity), we have

$$p_1 = \frac{2\pi}{L}[l, 0, 0, 0], \tag{2.7}$$

$$p_2 = \frac{2\pi}{L}[m, n, 0, 0], \tag{2.8}$$

where l, m, and n are dimensionless (they are the Fourier modes if they are chosen to be integers). In order to obtain any desired value of μ and ω we take advantage of (partially) twisted boundary conditions, which allow l, m, and n to be any real numbers. For any pair (μ, ω), the numbers (l, m, n) can be obtained from the kinematic constraints $p_1^2 = p_2^2 = \mu^2$ and $q^2 = \omega\mu^2$ by solving

$$\mu = 2\pi l/L, \tag{2.9}$$

$$l^2 = m^2 + n^2, \tag{2.10}$$

$$\omega l^2 = (l - m)^2 + n^2. \tag{2.11}$$

In order to show a concrete example, let us anticipate and consider one of the ensembles used in this work, with

spatial extent of $L/a = 32$ and inverse lattice spacing of $a^{-1} = 2.383(9)$ GeV. In that case, we can see that the following choice,

$$p_1 = \frac{2\pi}{L}[2.1372, 0, 0, 0], \tag{2.12}$$

$$p_2 = \frac{2\pi}{L}[1.60291, 1.41363, 0, 0], \tag{2.13}$$

corresponds to $\mu = 1$ GeV and $\omega = 0.5$ with an uncertainty at the per-mille level.

It is worth noting another choice of kinematics given by[2]

$$p_1 = \frac{2\pi}{L}[m, m, m, m], \tag{2.14}$$

$$p_2 = \frac{2\pi}{L}[\pm m, \pm m, \pm m, \pm m]. \tag{2.15}$$

Depending on the number of minus signs in p_2, we can obtain any integer value of ω between 0 and 4. With this choice we also expect the quark wave renormalization factor so to have similar lattice artifacts, whereas in the setup mentioned above they will have different discretization effects (except in some special cases). In that case, one can expect the discretization effects to be ω independent. We note that the same procedure with fewer than four components can lead to a noninteger value of ω: if the last component is fixed to zero, we can achieve the values $\omega = 0, 4/3, 8/3, 4$.

In this work we only consider the setup given in Eqs. (2.1)–(2.2) as we also want to investigate arbitrary noninteger values of ω. We chose to vary ω between 0.5 and 4 with a step of $1/2$. In addition, we can use the ω dependence of the discretization effects to obtain an additional handle to estimate the systematic uncertainties.

III. IMPLEMENTATION

A. Lattice implementation

For the bilinears, omitting flavor and spin-color indices for clarity (we only consider flavor nonsinglet operators) we define $O_\Gamma = \bar{\psi}\Gamma\psi$, with $\Gamma = \mathbb{1}, \gamma_\mu, \gamma_\mu\gamma_5, \gamma_5$ (S,V,A,P). We sketch here the computation of the propagators and of the bilinears needed to renormalize the quark mass and the quark wave function. We drop the volume factors and set $a = 1$ for simplicity.

Following [22], the momentum source propagators are computed by first solving

$$\sum_x D(y, x)\tilde{G}_x(p) = e^{ip.y}\mathbb{1}, \tag{3.1}$$

for a given momentum p, on Landau-gauged fixed configurations. In the previous equation, D denotes a generic Dirac matrix in spin-color space, regardless of the lattice discretization. Then we obtain the momentum source propagators by multiplying by the corresponding phase factor

$$G_x(p) = \tilde{G}_x(p)e^{-ip.x} = \sum_z D^{-1}(x, z)e^{ip.(z-x)}. \tag{3.2}$$

So within our conventions, $G_x(p)$ is an incoming propagator (with respect to x) with momentum p. After gauge average, the outgoing one is then given by $G_x(-p) = \gamma_5 G_x(p)^\dagger\gamma_5$. The advantage of the method proposed in [22] compared to a traditional Fourier transom is that there sum over z in Eq. (3.2) significantly reduces the statistical uncertainties. For the bilinears, we consider the diagram shown in Fig 1 and compute ($\langle\ldots\rangle$ denotes the gauge average)

$$V_\Gamma(p_2, p_1) = \langle\psi(p_2)O_\Gamma\bar{\psi}(p_1)\rangle, \tag{3.3}$$

$$= \sum_x \langle G_x(-p_2)\Gamma G_x(p_1)\rangle. \tag{3.4}$$

Defining $G(p) = \sum_x G_x(p)$, we then amputate the external legs

$$\Pi_\Gamma = \langle G^{-1}(-p_2)\rangle V_\Gamma(p_2, p_1)\langle G^{-1}(p_1)\rangle. \tag{3.5}$$

This quantity Π_Γ is obviously a matrix in spin-color space, the renormalization factors Z_Γ are then defined by projecting it to the corresponding tree-level value. A possible choice (which defines a so-called γ_μ scheme) is to use the same Γ matrix as in the vertex

$$\Lambda_\Gamma = \frac{1}{F}\mathcal{P}[\Pi_\Gamma] = \frac{1}{F}\text{Tr}[\Gamma\Pi_\Gamma], \tag{3.6}$$

where the trace is taken in color space and F is the corresponding tree-level value.

B. Z factors

Let us now specify our conventions for the renormalization factors. We denote the renormalized quantities with an index R, whereas the bare quantities do not carry extra indices. The quark wave function renormalization factor Z_q is defined by $\psi_R = \sqrt{Z_q}\psi$, and $G_R = Z_q G$ represents the renormalized fermion propagator. For the bilinears defined above, the renormalized quantities are denoted by $O_\Gamma^R = Z_\Gamma O_\Gamma$. Note that for the corresponding Green's functions, we have as usual $\Pi_\Gamma^R = Z_\Gamma/Z_q \times \Pi_\Gamma$.

The renormalization factors for the bilinears are then obtained by imposing

$$\lim_{m\to 0} \frac{Z_\Gamma(\mu, \omega)}{Z_q(\mu)} \times \Lambda_\Gamma\big|_{(\mu^2=p_1^2=p_2^2, (p_1-p_2)^2=\omega\mu^2)} = 1, \tag{3.7}$$

---

[2]Here we assume for simplicity that T = L, but in general the time component should be rescaled if this is not the case.

where m is the (bare) quark mass (before taking the chiral limit, we work with degenerate quark masses for simplicity). Note that we could take also the chiral limit by sending the renormalized mass to zero, here we assume that there is no additive mass renormalization.[3] There are several possible ways to define the quark field renormalization constant Z_q. For example in RI′/MOM, one imposes a condition directly on the fermionic propagator

$$Z_q(\mu) = -i \lim_{m \to 0} \left[\frac{1}{12p^2} \text{Tr}[\not{p} G^{-1}(p)] \right]_{\mu^2 = p^2}. \quad (3.8)$$

We now turn to the quark mass. The choice of the field renormalization fixes the renormalization factor Z_m, which relates the bare and renormalized masses as $m_R = Z_m m$. To be specific, we write in Fourier space the inverse bare fermion propagator

$$G^{-1}(p) = i\not{p} + m + \Sigma = i\not{p}(1 + \Sigma^V) + m(1 + \Sigma^S), \quad (3.9)$$

and similarly, having a generic MOM scheme in mind, we write for the renormalized propagator,

$$G_R^{-1}(p) = i\not{p} + m_R + \Sigma_R = i\not{p}(1 + \Sigma_R^V) + m_R(1 + \Sigma_R^S). \quad (3.10)$$

Since $G_R = Z_q G$, we have

$$(1 + \Sigma_R^V) = Z_q^{-1}(1 + \Sigma^V), \quad (3.11)$$

$$(1 + \Sigma_R^S) = Z_q^{-1} Z_m^{-1}(1 + \Sigma^S). \quad (3.12)$$

Traditionally in a MOM scheme, one defines the renormalization factors Z_m and Z_q by imposing that the renormalized parts are finite in the chiral limit at a certain renormalization point. For example the renormalization factor Z_m can then be extracted from

$$Z_m(\mu) = \frac{1}{Z_q(\mu)} \lim_{m \to 0} \left[\frac{1}{12m} \text{Tr}[G^{-1}(p)] \right]_{\mu^2 = p^2}, \quad (3.13)$$

which is equivalent to

$$\lim_{m \to 0} \left[\frac{1}{12m_R} \text{Tr}[G_R^{-1}(p)] \right]_{\mu^2 = p^2} = 1. \quad (3.14)$$

In [9], it was suggested to replace this condition by

$$\lim_{m \to 0} \left\{ \frac{1}{12m_R} \left[\text{Tr}[G_R^{-1}(p)]_{\mu^2 = p^2} - \frac{i}{2} \text{Tr}[q_\mu \Pi_{A,R}^\mu \gamma_5]_{\mu^2 = p_1^2 = p_2^2 = (p_1 - p_2)^2} \right] \right\} = 1. \quad (3.15)$$

The motivation for this definition of Z_m is that it leads to $Z_m = 1/Z_P$ if Z_P is defined from Eq. (3.6) at the same kinematic point. This follows from requiring that the Ward-Takahashi identities (WTI) given below are satisfied both for the bare and renormalized quantities (for degenerate quark masses)

$$q_\mu \Pi_{V^\mu}(p_1, p_2) = -i(G^{-1}(p_2) - G^{-1}(p_1)), \quad (3.16)$$

$$q_\mu \Pi_{A^\mu}(p_1, p_2) = 2im\Pi_P(p_1, p_1) - i(\gamma_5 G^{-1}(p_2) + G^{-1}(p_1)\gamma_5), \quad (3.17)$$

in the case of degenerate quark masses. Imposing this condition with the SMOM kinematics leads to maintaining the WTI on the renormalized quantities. In particular the procedure leads to $Z_A = Z_V$.

C. Our definitions

We deviate from the choice made in [9] for several reasons. Firstly, some derivations in [9] rely on the SMOM kinematics, which we want to generalize here. Secondly, rather than imposing the renormalization conditions directly on the quark propagators, we prefer to extract the renormalization factors from the bilinears. In this paper we are using domain wall fermions, so we assume that $Z_A = Z_V$, whose values are known from previous studies on the same lattice, and are given in Appendix B for convenience. (The deviation Z_V/Z_A from one is studied in Appendix 4.6.) Additionally, we define Z_m directly as

$$Z_m = 1/Z_S, \quad (3.18)$$

and we also define

$$\frac{Z_V}{Z_q(\mu, \omega)} \lim_{m \to 0} [\Lambda_V]_{\text{IMOM}} = 1, \quad (3.19)$$

$$\frac{Z_S(\mu, \omega)}{Z_q(\mu, \omega)} \lim_{m \to 0} [\Lambda_S]_{\text{IMOM}} = 1, \quad (3.20)$$

---

[3]With domain-wall fermions, a small additive renormalization of the quark mass is also necessary. For simplicity we also assume the residual mass has already been included; here the quark mass renormalizes multiplicatively.
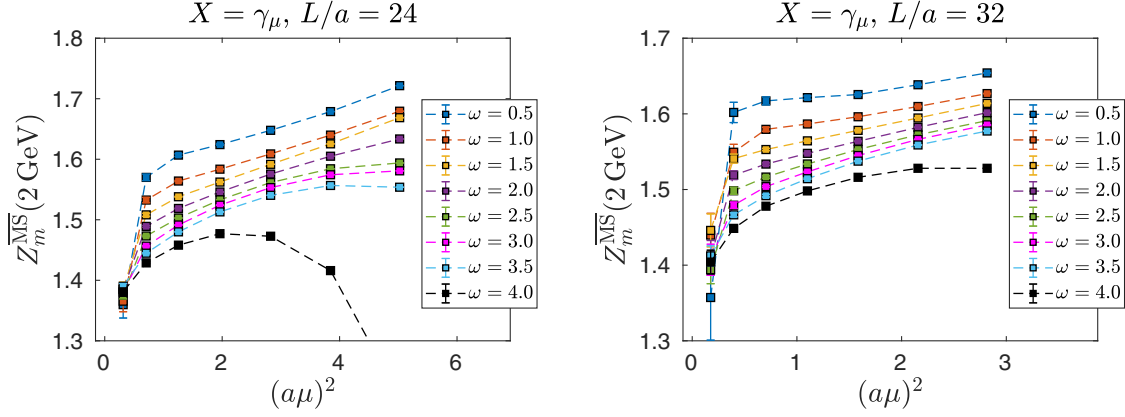
FIG. 3. Z_m at $\mu = 2$ GeV in $\overline{\text{MS}}$, converted using NNLO. The results are shown as a function of the square of the momentum scale at which the renormalization factors are nonperturbatively extracted.

where the shorthand IMOM stands for $\mu^2 = p_1^2 = p_2^2$, $(p_1 - p_2)^2 = \omega\mu^2$. (These equations are used for the quark wave function and the mass renormalization factors.) More explicitly, we define

$$Z_q(\mu, \omega) = Z_V \lim_{m \to 0} [\Lambda_V]_{\text{IMOM}}, \tag{3.21}$$

$$Z_m(\mu, \omega) = \frac{1}{Z_V} \lim_{m \to 0} \left[\frac{\Lambda_S}{\Lambda_V}\right]_{\text{IMOM}}, \tag{3.22}$$

where $\Lambda_{V,S}$ are the bare (and local) vertices defined above. Note that both Z_m and Z_q acquire an ω dependence through these definitions. This dependence is discussed in Sec. IV. The main advantage of this approach is that the Green's functions of the bilinears have a much safer infrared behavior than the quark propagators.

In order to completely fix the definition of Z_q and Z_m in Eqs. (3.21) and (3.22) we need to specify our the choice of projector $\mathcal{P}_\mu$ for the vector Green's function,

$$\Lambda_V = \frac{1}{F} \mathcal{P}_\mu [\Pi_{V^\mu}]. \tag{3.23}$$

We implement the so-called γ_μ and $\not{q}$ projectors (the trace is taken over both Dirac and color indices)

$$\Lambda_V^{(\gamma_\mu)} = \frac{1}{48} \text{Tr}[\gamma_\mu \Pi_{V^\mu}], \tag{3.24}$$

$$\Lambda_V^{(\not{q})} = \frac{q^\mu}{12q^2} \text{Tr}[\not{q} \Pi_{V^\mu}], \tag{3.25}$$

where obviously $q = p_1 - p_2$ is the momentum transfer of the IMOM kinematic defined above, $\mu^2 = p_1^2 = p_2^2$, $(p_1 - p_2)^2 = \omega\mu^2$. Plugging these definitions in Eqs. (3.21) and (3.22), we see that we have defined two kinds of IMOM schemes similarly to what was done in the SMOM case. In order to keep track of what projector was

used, we introduce the respective notations $Z_m^{(\gamma_\mu)}(\mu, \omega)$ and $Z_m^{(\not{q})}(\mu, \omega)$ for the renormalization factors.

The renormalization factors for the other bilinears are defined exactly in the same way as Eqs. (3.19) and (3.20). This, together with a lattice formulation which preserves chiral symmetry, leads to $Z_V = Z_A$ and $Z_S = Z_P$, apart from the physical effects of spontaneous chiral symmetry breaking, which may become important at low p^2 and q^2. This is discussed in Sec. IV. Naturally for a lattice formulation which breaks explicitly chiral symmetry, one can follow [9] with the modification $q^2 = \omega\mu^2$.

D. Nomenclature

To define unambiguously a momentum scheme for a composite operator one needs to specify the kinematics (the choice of momenta) and the choice of projectors, not only for the Green's function corresponding to the operator in question, but also for the quark wave function.[4] Historically, when the Rome-Southampton method was introduced in [3], the kinematics was the exceptional case, $p_1 = p_2$ and Z_q was defined through a γ_μ projector, i.e. Eq. (3.24). Although the authors of [3] mentioned explicitly that other choices were possible, by convention "RI/MOM scheme" refers to this specific choice of kinematics and wave function. Similarly, it also became standard to call "RI′/MOM scheme" a scheme in which the kinematics is also exceptional ($p_1 = p_2$) but the quark wave function is renormalized through a $\not{q}$ projector, i.e. Eq. (3.25). (In [3] the definition of the projector differs from the one given here, but both definitions are equivalent up to lattice artifacts).

We turn now to the SMOM schemes. By definition, the S of SMOM refers to the situation where $p_1^2 = p_2^2 = (p_1 - p_2)^2$, i.e. $\omega = 1$, or "symmetric" [9]. For the quark

---

[4]Strictly speaking we also need to specify the gauge, but it is standard to assume that the computation is performed in the Landau gauge.

wave function, the convention in [9] was that RI/SMOM refers to a $\not{q}$ projector and RI/SMOM$_{\gamma_\mu}$ to a γ_μ projector. There is also a similar subtlety in the definition of Z_m, see Sec. III B.

Here, following the conventions adopted by RBC-UKQCD (see for example [8]), we use the notations $Z^{(X)}(\mu, \omega)$, where $X \in \{\gamma_\mu, \not{q}\}$ indicates the choice of the projector for the wave function. Obviously the choice of kinematics is explicitly given by ω. When needed, we also refer to these schemes as IMOM$^{(\gamma_\mu)}$ and IMOM$^{(\not{q})}$.

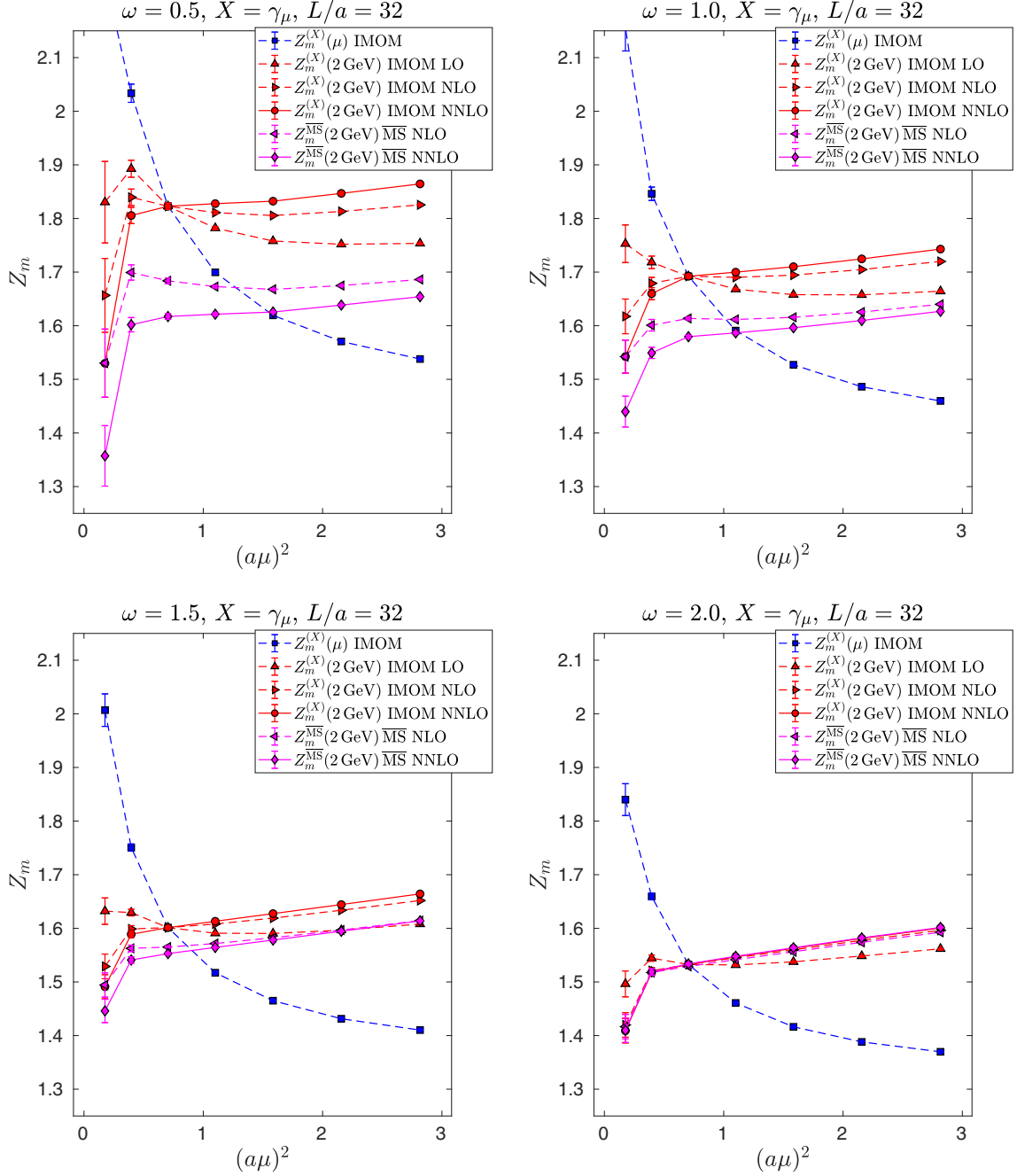| Name	Kinematics	Projector for Z_q
RI/MOM	$p_1 = p_2$	γ_μ
RI′/MOM	$p_1 = p_2$	$\not{q}$
RI/SMOM$_{\gamma_\mu}$	$p_1^2 = p_2^2 = (p_1 - p_2)^2$	γ_μ
RI/SMOM	$p_1^2 = p_2^2 = (p_1 - p_2)^2$	$\not{q}$
IMOM$^{(\gamma_\mu)}$	$p_1^2 = p_2^2 = \mu^2, (p_1 - p_2)^2 = \omega\mu^2$	γ_μ
IMOM$^{(\not{q})}$	$p_1^2 = p_2^2 = \mu^2, (p_1 - p_2)^2 = \omega\mu^2$	$\not{q}$

FIG. 4. Z_m at $\mu = 2$ GeV in $\overline{\text{MS}}$ converted from $X = \gamma_\mu$ and for $\omega = 0.5, 1.0, 1.5, 2.0$.

IV. RESULTS

A. A first look at Z_m

For clarity we assume here that the Z factors are taken in the chiral limit. (We find that the chiral extrapolations are well under control; they are shown in Appendix C.) In Fig. 3 we show our results for $Z_m^{\overline{\text{MS}}}$ computed at 2 GeV for the various values of ω and for the two different values of the lattice spacing. We start by computing $Z_m^{(\gamma_\mu)}(\mu, \omega)$ for the different values

of (μ, ω), then we run perturbatively to the reference scale of 2 GeV and finally match to $\overline{\text{MS}}$ using NNLO at fixed ω. This can written as

$$Z_m^{(\gamma_\mu)}(2 \text{ GeV}, \omega) = U_m^{(\gamma_\mu)}(2 \text{ GeV}, \mu, \omega, \omega_0)|_{\omega=\omega_0} Z_m^{(\gamma_\mu)}(\mu, \omega),$$
$$(4.1)$$

$$Z_m^{\overline{\text{MS}}}(2 \text{ GeV}) = C_m^{(\gamma_\mu)}(2 \text{ GeV}, \omega) Z_m^{(\gamma_\mu)}(2 \text{ GeV}, \omega). \quad (4.2)$$
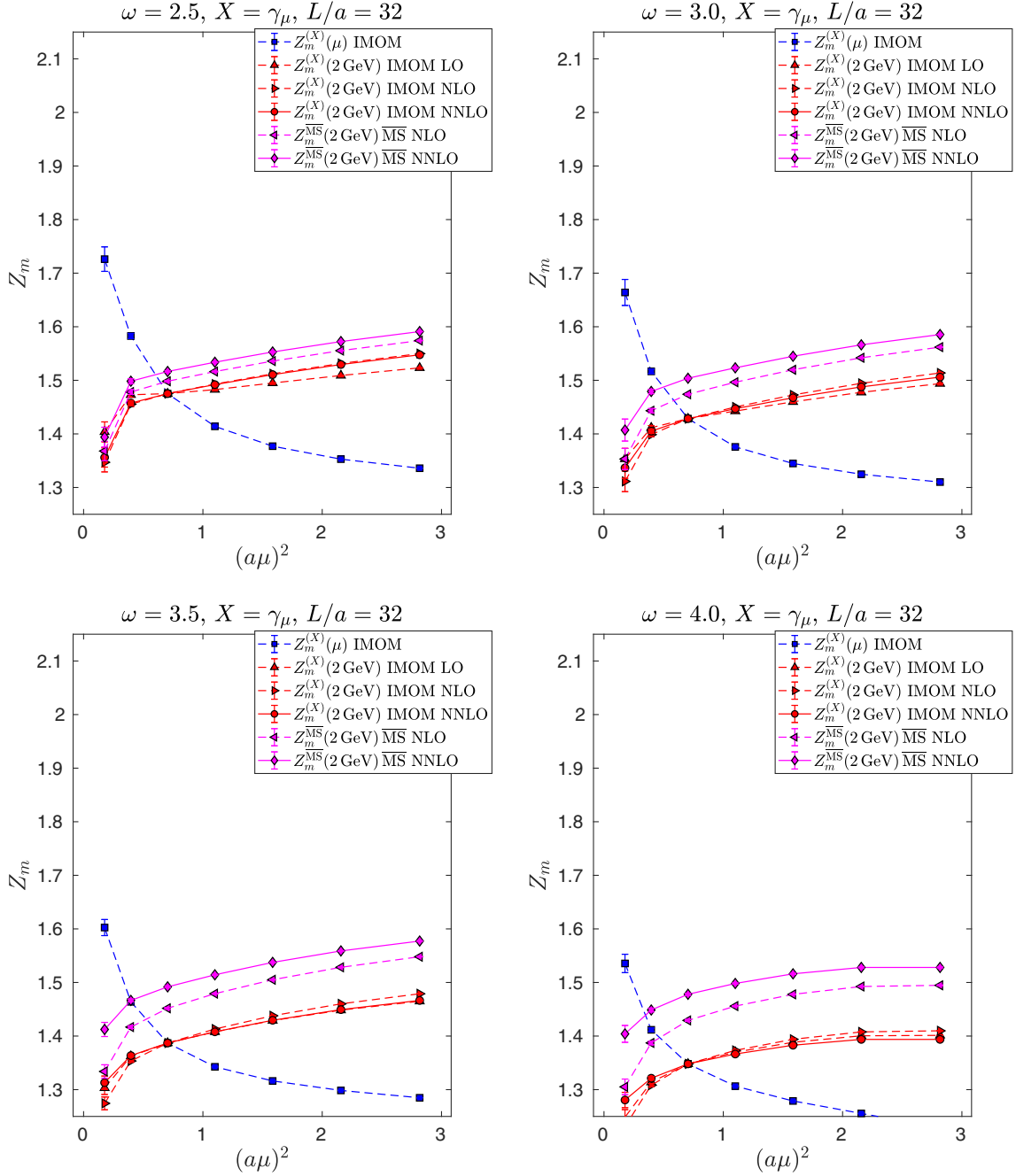

FIG. 5. Same as Fig. 4 for $\omega = 2.5, 3.0, 3.5, 4.0$.

Although the notations should be self-explanatory, the precise definitions of the matching and running coefficients are given in Appendix A (we assume $\nu = \mu$ and do not repeat the corresponding index for clarity). Our

results are shown versus the square of the lattice momentum $(ap)^2 = (a\mu)^2$ for fixed values of ω in Figs. 4 and 5. The blue squares show $Z_m^{(\gamma_\mu)}(\mu, \omega)$ for the different values of the renormalization scale (at this
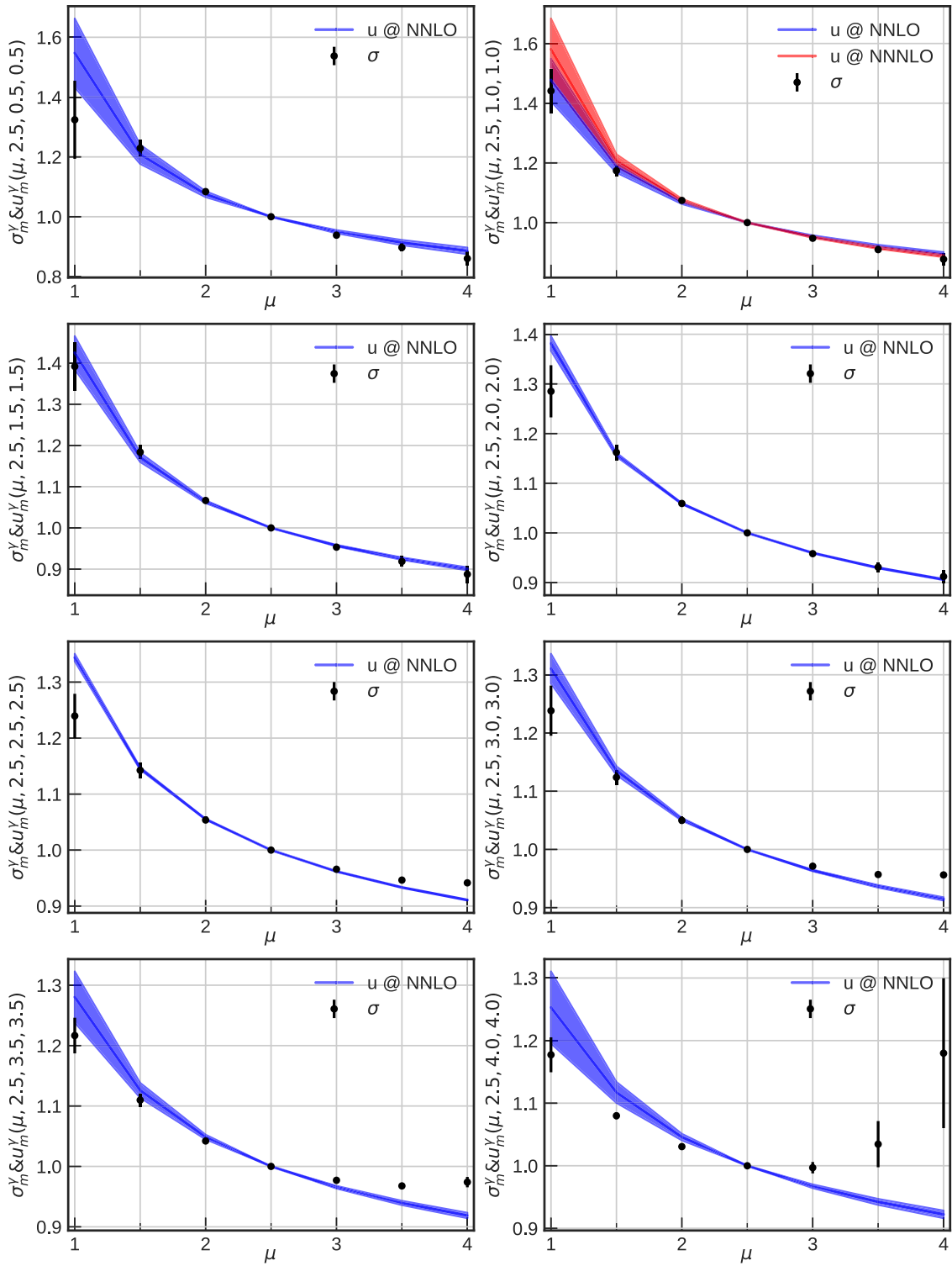
FIG. 6. Comparison of the nonperturbative and perturbative running for $Z_m^{(\gamma_\mu)}$. Note that for $\omega = 1$ the perturbative running is known at N^{3}LO.

point no perturbation theory is used). Then for each value of μ, we run to 2 GeV, using the perturbative predictions at LO, NLO, and NNLO, still in the IMOM scheme (red points), as in Eq. (4.1). Finally

we convert this renormalization factor to $\overline{\rm MS}$ at 2 GeV (magenta), see Eq. (4.2). As expected, the large values of ω and $(a\mu)^2$ are more affected by discretization effects. The extreme value $\omega = 4$ is just shown here for

FIG. 7. Same as Fig. 6 for $Z_m^{(q)}$.

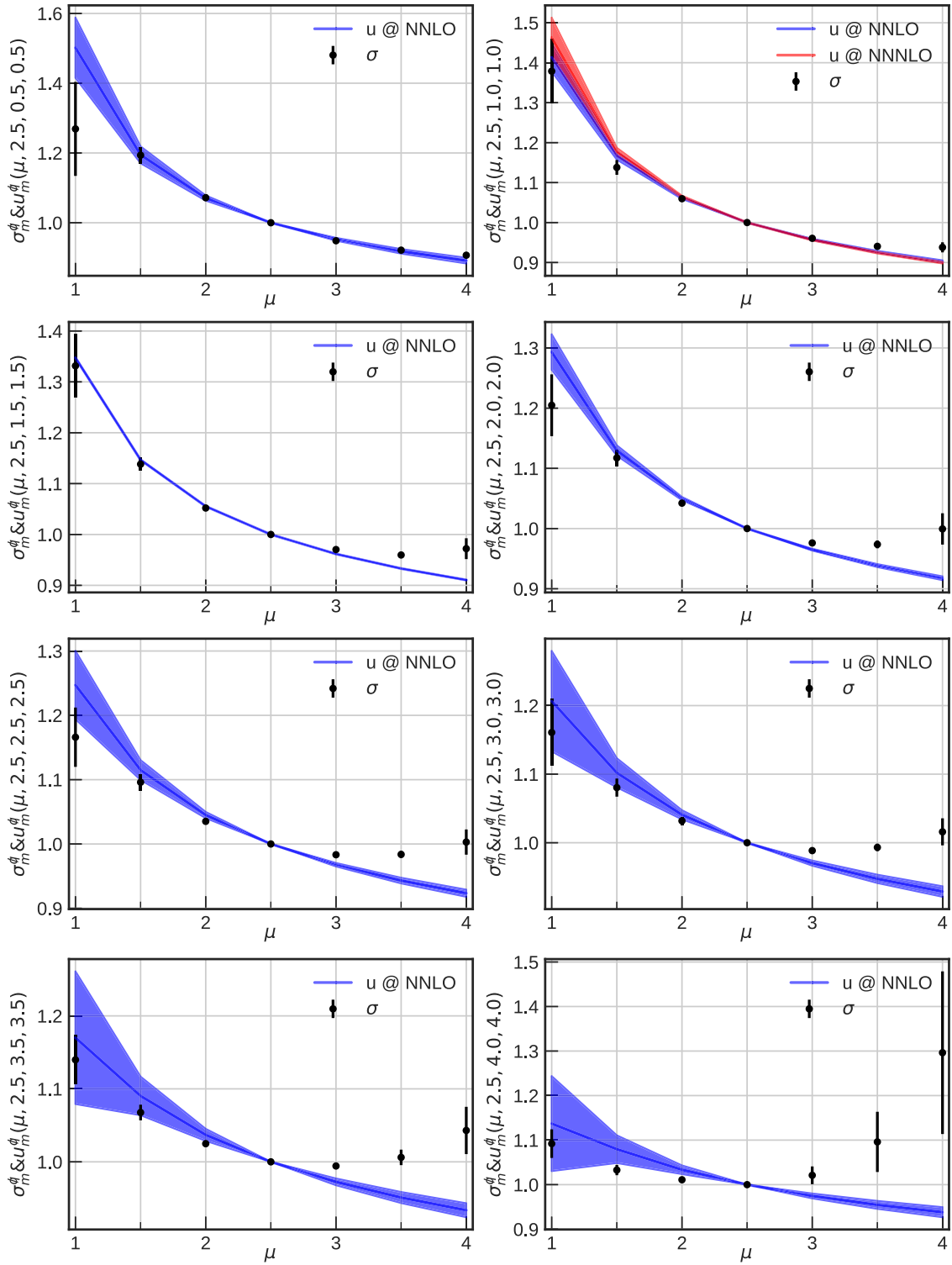illustration. It is clear from Fig. 3 that, even on our finest lattice, there is still an $(a\mu)^2$ and ω dependence after conversion. This is not unexpected since these quantities have different discretization effects and different perturbative uncertainties. We also show a similar analysis for $X = \not{q}$ in Appendix D, Fig. 22; our conclusions remain the same, although $\omega \sim 1$ appears to be better for $\not{q}$ while γ_μ favors $\omega \sim 2$ for this quantity.

From this analysis, we conclude that the bulk of the renormalization scale dependence is well described by perturbation theory as long as ω remains moderate. However it is clear that our results are affected by systematic errors (as expected) and a more refined analysis is required in order to disentangle the various effects. Furthermore we observe that for this quantity our data favor

$\omega = 2$ for $X = \gamma_\mu$, where the systematic errors are significantly less pronounced.

B. Strategy and nonperturbative running

In practice, we want to perform the computation nonperturbatively on the lattice at several values of the lattice spacing, take the chiral and continuum limit and then apply (continuous) perturbation theory. So the strategy is to compute the Z factors at a given scale μ (fixed in physical units) in the chiral limit, for a fixed value of ω and for each lattice spacing a in the corresponding IMOM scheme. The extrapolation to the continuum can be performed once the corresponding bare quantity has been computed at the same values of the lattice spacing a. In a nutshell, the strategy reads (omitting the chiral extrapolation for clarity) [16,17]
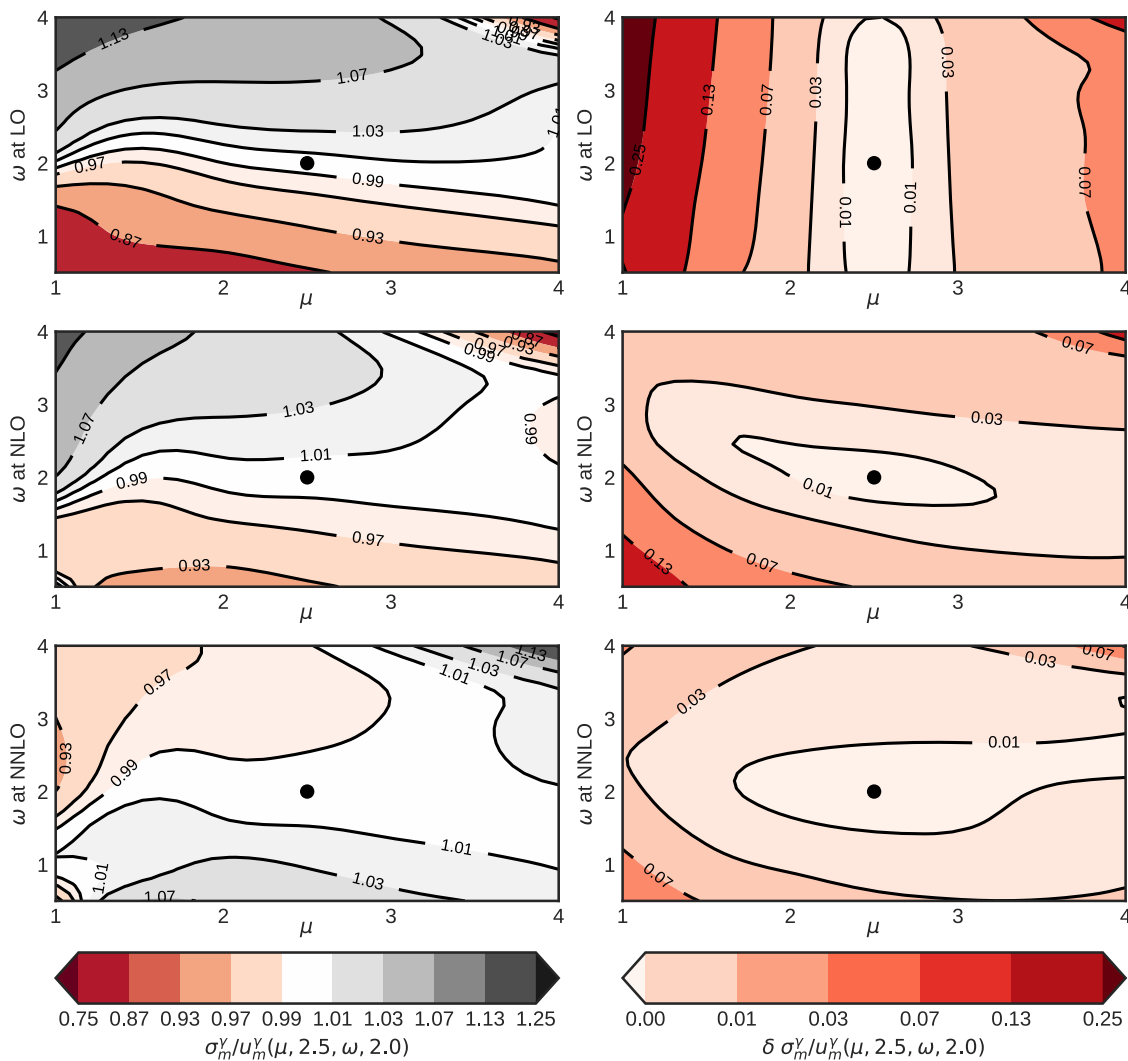

FIG. 8. Ratio of the nonperturbative running over the perturbative prediction for $Z_m^{(\gamma_\mu)}$. The central value is shown on the left and the error on the right. This ratio is exactly one (by definition) for the point ($\mu = 2.5$ GeV, $\omega = 2$).

$$\text{(step 1)} \quad O^{\text{IMOM},(X)}(\mu, \omega) = \lim_{a^2 \to 0} Z^{\text{IMOM},(X)}(\mu, \omega, a^2) O^{\text{bare}}(a^2), \tag{4.3}$$

$$\text{(step 2)} \quad O^{\overline{\text{MS}}}(\mu) = C(\mu, \omega)^{\text{IMOM},(X)} O^{\text{IMOM},(X)}(\mu, \omega), \tag{4.4}$$

where X denotes the projector used in the defining of IMOM. Clearly the first step is purely nonperturbative and can be used to assess the size of the discretization artifacts. On the other hand, the second step is performed in the continuum and can be used to estimate the size of the perturbative uncertainties.

In this work, we are only concerned with renormalization factors and do not want to introduce bare quantities. However we still want to disentangle the lattice discretization artifacts from the perturbative errors. It is therefore natural to consider the nonperturbative scale evolution of Z_m. In the spirit of [15], we define Σ_m as

$$\Sigma_m^{(X)}(a^2, \mu, \mu_0, \omega, \omega_0) = \lim_{m \to 0} \frac{Z_m^{(X)}(a^2, \mu, \omega)}{Z_m^{(X)}(a^2, \mu_0, \omega_0)}, \tag{4.5}$$

where X can either be γ_μ or $\slashed{q}$. We can then take the continuum limit $a^2 \to 0$ and define

$$\sigma_m^{(X)}(\mu, \mu_0, \omega, \omega_0) = \lim_{a^2 \to 0} \Sigma_m^{(X)}(a^2, \mu, \mu_0, \omega, \omega_0). \tag{4.6}$$

Similarly, for the quark wave function we define σ_q, by just substituting Z_q for Z_m in the above definitions. We note that
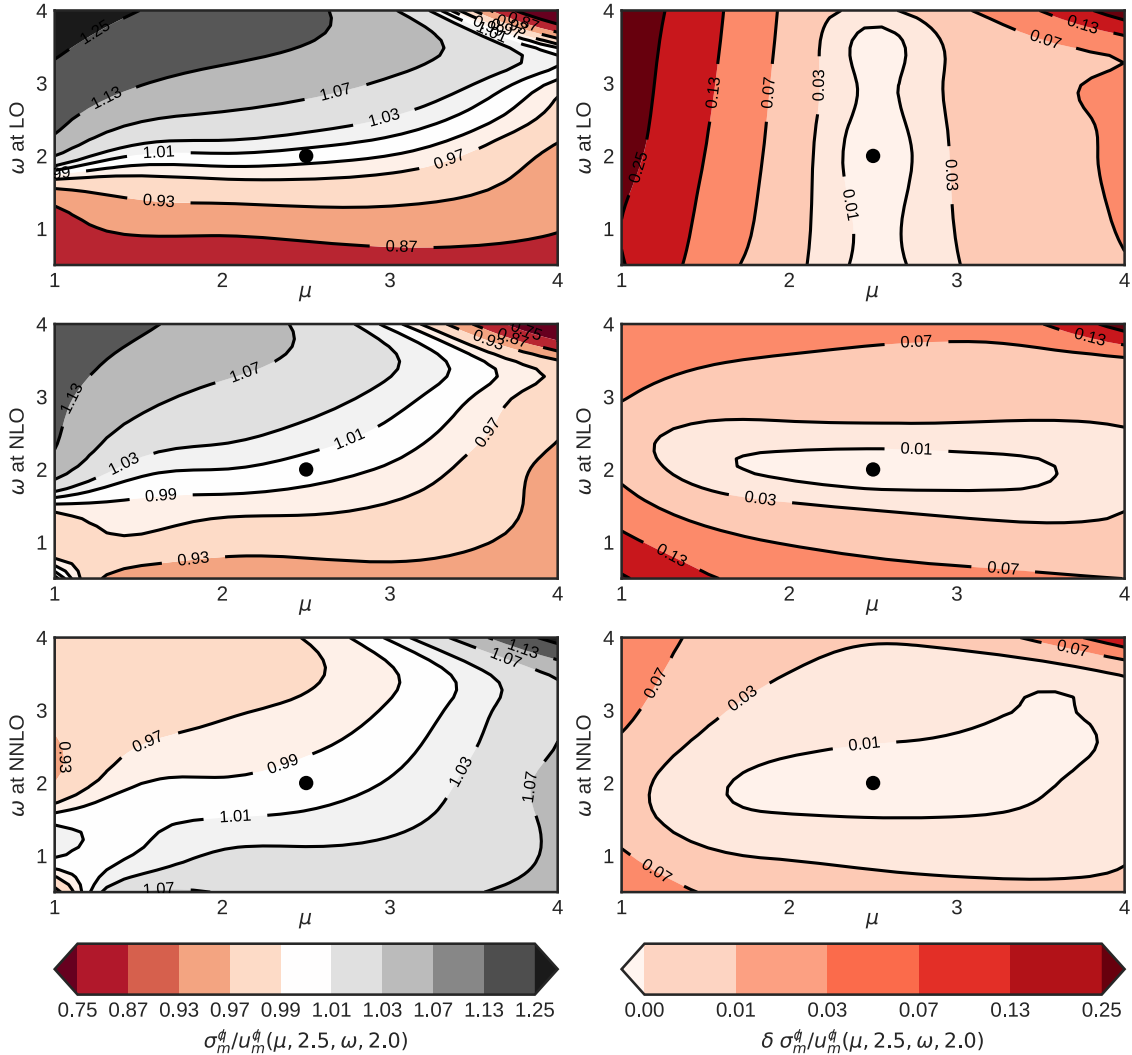

FIG. 9. Same as Fig. 8 for $Z_m^{(\slashed{q})}$.

TABLE I. Running between 2 and 2.5 GeV for the quark mass. First we perform the computation directly in $\overline{\text{MS}}$ then and in the SMOM ($\omega = 1$) schemes γ_μ and $\not{q}$. In this case the running is known at NNNLO (N³LO). The lattice results are denoted by NP (nonperturbative). We also show the running computed first nonperturbatively then converted to $\overline{\text{MS}}$; we denote them by $\overline{\text{MS}} \leftarrow \gamma_\mu$ and $\overline{\text{MS}} \leftarrow \not{q}$, respectively.

Scheme	LO	NLO	NNLO	NNNLO	NP
$\overline{\text{MS}}$	0.9537	0.9456	0.9441	0.9439	
$\overline{\text{MS}} \leftarrow \gamma_\mu$	0.9537	0.9350	0.9389	0.9426	
$\overline{\text{MS}} \leftarrow \not{q}$	0.9537	0.9451	0.9462	0.9475	
γ_μ	0.9537	0.9411	0.9357	0.9318	0.9307(62)
$\not{q}$	0.9537	0.9441	0.9415	0.9400	0.9436(46)

TABLE II. Study of the convergence of the perturbative series for running of the quark mass between 2 and 2.5 GeV in $\overline{\text{MS}}$, SMOM-γ_μ, and $\not{q}$.

Scheme	NLO-LO	NNLO-NLO	NNNLO-NNLO
$\overline{\text{MS}}$	−0.0081	−0.0015	−0.0002
γ_μ	−0.0126	−0.0054	−0.0040
$\not{q}$	−0.0096	−0.0026	−0.0017

we cannot only run in the μ direction but also in the ω direction by setting $\omega \neq \omega_0$.

In this work, we only consider two values of the lattice spacing; therefore, we add a systematic error as an estimate of the residual discretization errors. This error is obtained

by adding half the difference between the extrapolated value and the value on the finest lattice spacing. The continuum extrapolations can be found in Appendix F. We now have, for each value of μ, μ_0, ω, ω_0, a central value of $\sigma_{\{m,q\}}$, a statistical error and a systematic error from the continuum extrapolation. In the following we will always sum the systematic and statistical uncertainties in quadrature except when stated otherwise.

We can now compare the continuous nonperturbative running obtained from our lattice simulation with the perturbative prediction. This has to be done in a kinematic region where both perturbation theory and lattice results are reliable, the so-called Rome-Southampton windows. In this region the perturbative and lattice results should run in the same way, so the ratio should be constant. We will see deviations from constancy in regions where perturbation theory converges slowly (for example at small μ or small $q^2 = \omega\mu^2$). We will also see nonconstancy if lattice artifacts are important, which is likely to happen at large μ^2 and large $\omega\mu^2$. We also note that our procedure to estimate the residual discretization errors could potentially underestimate them in the large μ^2 and large $\omega\mu^2$ regions.

In the following sections we will first keep $\omega = \omega_0$ and compare the μ dependence of the lattice results and the continuum. An advantage of IMOM is that we have two parameters, μ and ω, so we can better test that we are working in a region where we can trust both perturbative and lattice results. Accordingly, we next will vary both μ and ω and study if a plateau is emerging where we can reliably determine the Z factors of interest.

TABLE III. Nonperturbative running for the quark mass in the γ_μ scheme.

$\omega/\mu =$	1.0	1.5	2.5	3.0	3.5	4.0
0.5	1.219(123)	1.131(21)	0.922(8)	0.866(13)	0.827(18)	0.793(26)
1.0	1.343(64)	1.092(16)	0.931(6)	0.882(11)	0.846(17)	0.816(24)
1.5	1.306(52)	1.110(12)	0.937(5)	0.894(11)	0.861(17)	0.831(25)
2.0	1.214(49)	1.099(11)	0.944(5)	0.904(10)	0.878(14)	0.860(17)
2.5	1.176(37)	1.085(9)	0.949(5)	0.916(9)	0.898(10)	0.893(7)
3.0	1.180(39)	1.070(7)	0.952(6)	0.925(8)	0.911(8)	0.910(4)
3.5	1.169(27)	1.065(6)	0.959(5)	0.937(6)	0.928(4)	0.935(5)
4.0	1.142(27)	1.049(5)	0.970(2)	0.968(10)	1.004(36)	1.144(116)

TABLE IV. Nonperturbative running for the quark mass in the $\not{q}$ scheme.

$\omega/\mu =$	1.0	1.5	2.5	3.0	3.5	4.0
0.5	1.182(128)	1.110(21)	0.933(8)	0.886(9)	0.860(8)	0.846(8)
1.0	1.302(73)	1.074(18)	0.944(5)	0.907(5)	0.888(4)	0.885(11)
1.5	1.266(57)	1.082(10)	0.951(3)	0.922(3)	0.912(3)	0.924(17)
2.0	1.157(49)	1.074(11)	0.959(4)	0.936(5)	0.933(4)	0.958(22)
2.5	1.127(43)	1.060(10)	0.966(5)	0.950(5)	0.950(3)	0.969(16)
3.0	1.126(45)	1.047(8)	0.969(5)	0.958(6)	0.962(3)	0.985(15)
3.5	1.114(32)	1.042(7)	0.976(4)	0.970(4)	0.982(7)	1.018(28)
4.0	1.080(30)	1.023(7)	0.989(6)	1.009(25)	1.081(71)	1.274(182)

C. Quark mass renormalization factor

The running of the quark mass is shown in Fig 6 for the γ_μ scheme and in Fig. 7 for the $\not{q}$ scheme. In these plots we show both the nonperturbative scale evolution

$\sigma_m^{(\gamma_\mu)}(\mu, \mu_0, \omega, \omega_0)$ and the perturbative prediction $u_m^{(\gamma_\mu)}(\mu, \mu_0, \omega, \omega_0)$. In order to study the μ evolution for fixed values of ω, we set $\omega = \omega_0 = 0.5, 1.0, 1.5, \ldots, 4.0$ and let μ vary between 1 and 4 GeV. We find a good
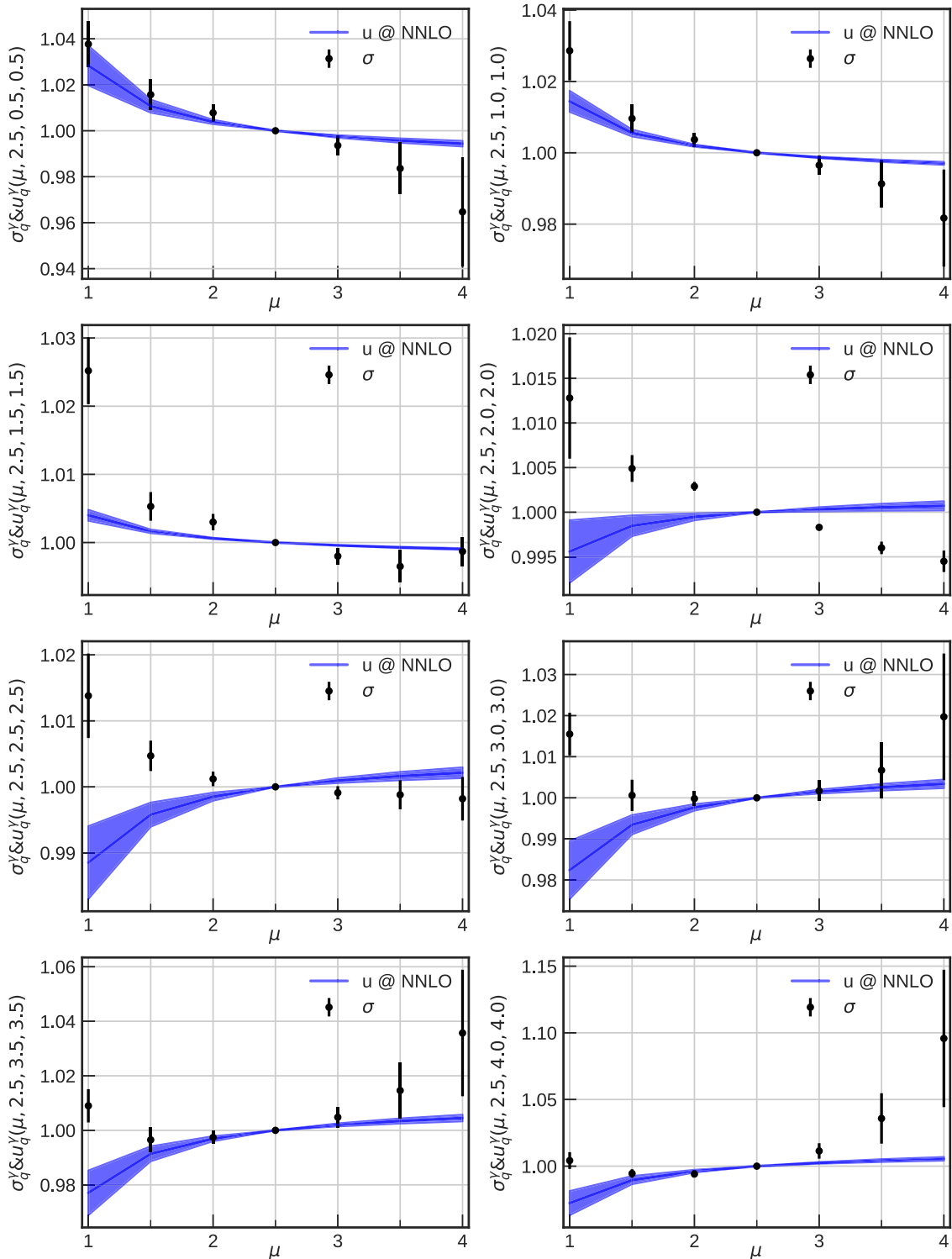
FIG. 10. Same as Fig. 6 for $Z_q^{(\gamma_\mu)}$.

agreement for intermediate values of μ and ω, where both perturbation theory and lattice artifacts are expected to be under good control. In fact, perturbation theory works surprisingly well even for small values of μ, where

significant discrepancies with the lattice results only emerge at $\mu \simeq 1$ GeV. Out of the two schemes, perturbation theory and lattice results agree best in the γ_μ scheme. The onset of lattice artifacts for large values of μ and ω becomes

FIG. 11. Same as Fig. 6 for $Z_q^{(q)}$.

FIG. 12. Same as Fig. 8 for $Z_q^{(\gamma_\mu)}$.

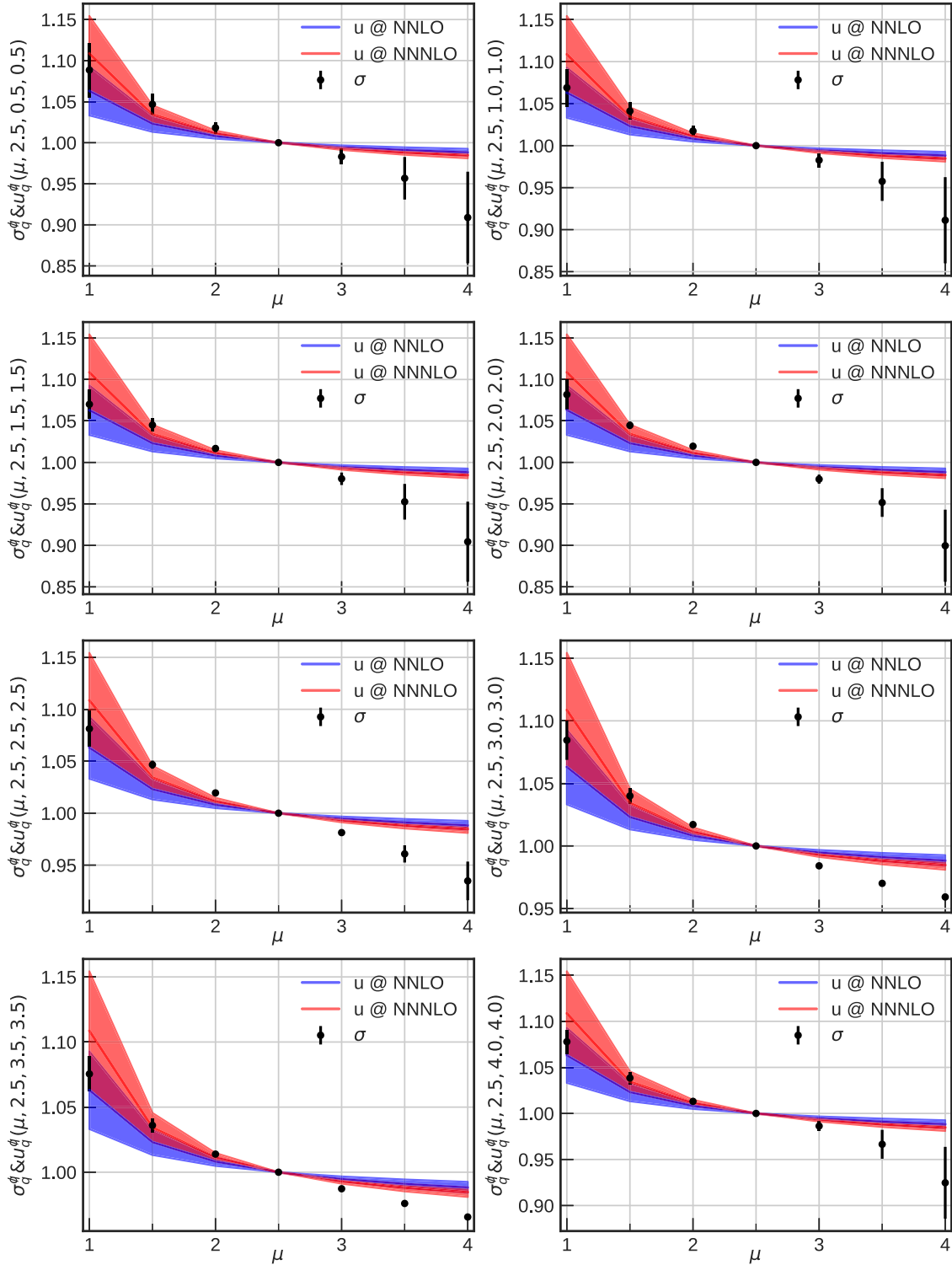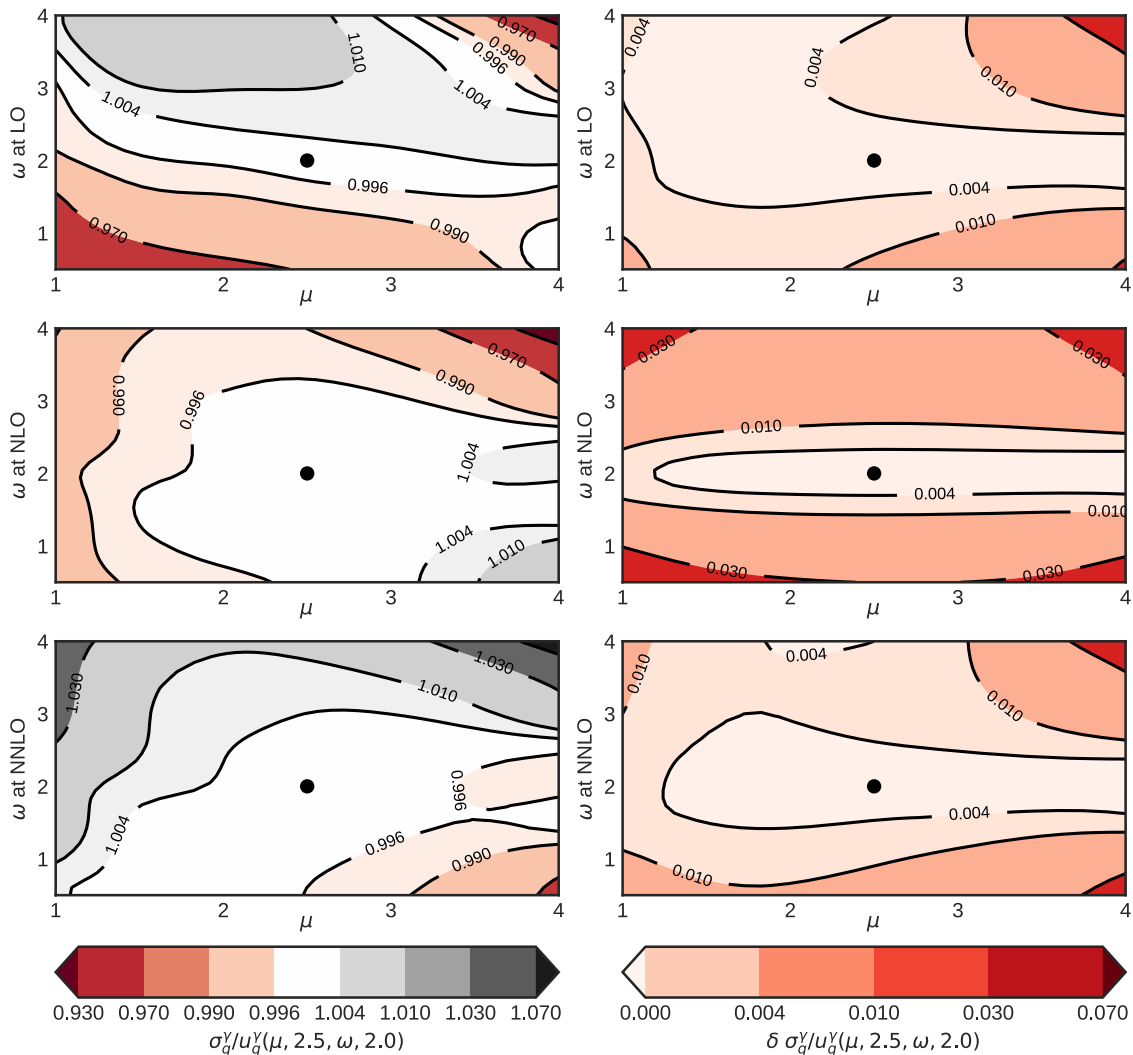only relevant for $q^2 \gtrsim 25$ GeV^2. This becomes particularly visible for large values of $\omega = 4$, where perturbation theory also becomes less reliable. The discrepancy of lattice results and perturbation theory occurs already at values of $q^2 \gtrsim 10$ GeV^2 in the $\not q$ scheme.

Next we allow $\omega \neq \omega_0$ and show the ratio of the nonperturbative running divided by the perturbative prediction as a function of μ and ω at LO, NLO, and NNLO. Here we choose to fix $\omega_0 = 2$ and $\mu_0 = 2.5$ GeV as a reference point. For $\mu = \mu_0$ and $\omega = \omega_0$ this ratio is one by definition, and ideally should stay close to one in the remainder of the (μ, ω) plane. We show our results for $X = \gamma_\mu$ in Fig. 8 and in Fig. 9 for $X = \not q$, where we also give the combined lattice and perturbative uncertainties (added in quadrature).

As expected, we observe that increasing the order of the perturbative expansion improves the agreement with the nonperturbative evolution. The corner of the planes are

affected by larger systematic errors, in particular where $\omega = 4$ and/or $\mu > 3.5$ GeV where the discretization effects become more sizeable. However our data agree with NNLO at a few percent level for a large part of the (μ, ω) plane: approximately for 1.5 GeV $\leq \mu \leq 3.5$ GeV and $1 \leq \omega \leq 3$.

For completeness, we study the next order in perturbation theory for the case $\omega = 1$, as the three-loop matching has been computed in [13,14] and the $\overline{\text{MS}}$ four-loop anomalous dimension can be found in [23]. We take $\mu_0 = 2$ GeV and $\mu = 2.5$ GeV and compute the running in different schemes, see Table I. In Table II, we show the contributions of the higher orders. Although the corrections to the leading order contributions are rather small, we see that the convergence in $\overline{\text{MS}}$ seems to be much better than in the MOM schemes, in the sense that the $(i + 1)$th correction is much smaller than the ith order. However, the important observations here are that the leading order gives by far the
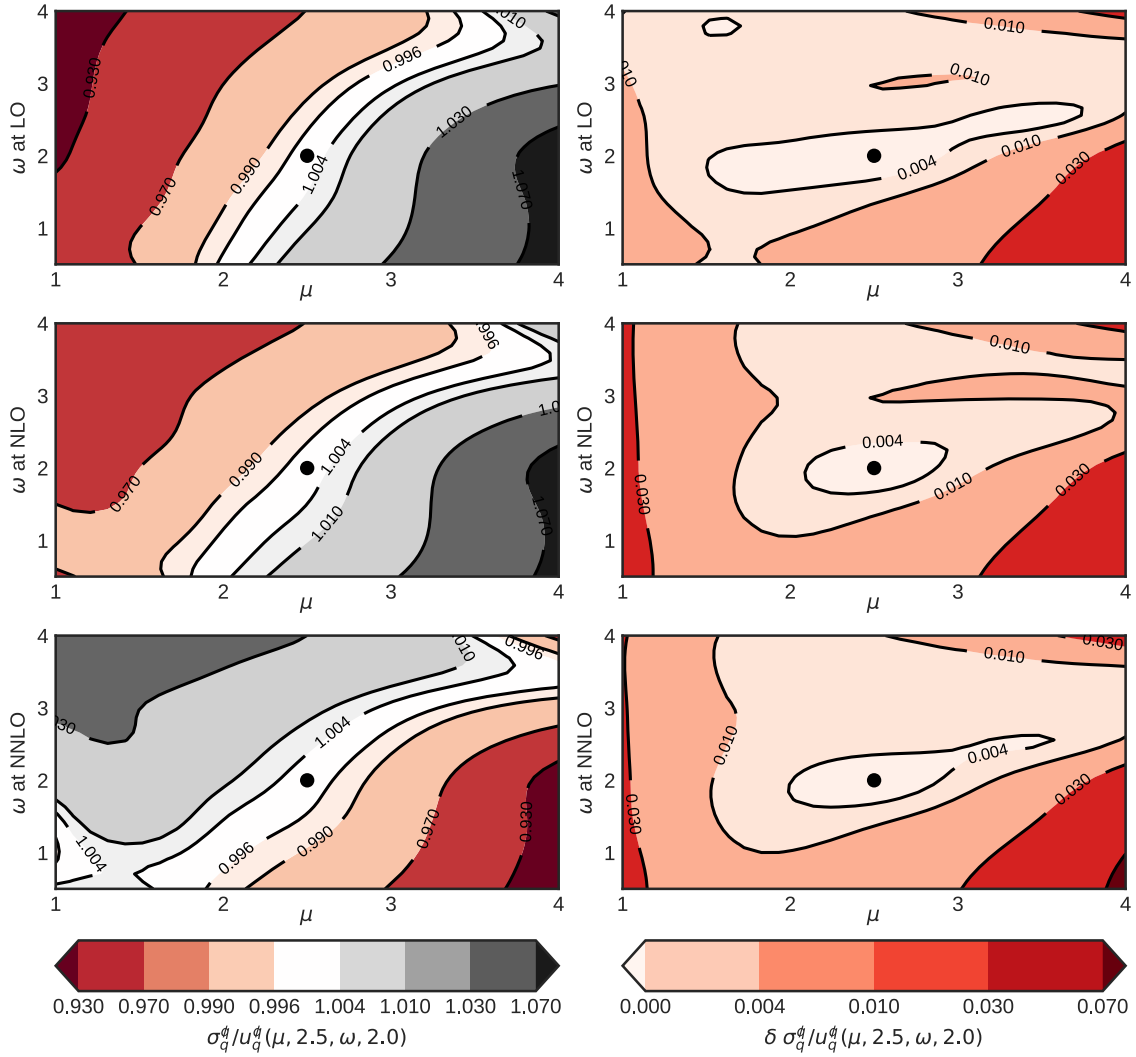
FIG. 13.   Same as Fig. 8 for $Z_q^{(\slashed{q})}$.

main contribution and that the perturbative series seems to converge nicely to the nonperturbative values.[5]

Finally for completeness, in Tables III and IV we give our results for the nonperturbative running of the quark mass, with $\mu_0 = 2$ GeV and $\omega = \omega_0$ varying between 0.5 and 4.0. In Appendix E, we show more numerical results, where we vary our parameters ω, ω_0, μ, and μ_0 in various ways. Our main conclusion remains that the nonperturbative results agree very well with the perturbative ones as long as we stay away from the corner of the (ω, μ) plane. However it is worth noting again that for $X = \gamma_\mu$, our data favor $\omega = 2$. From the contour plot, we conclude that in the region $1.5 \leq \omega \leq 2.5$ and $1.5 \leq \mu \leq 2.5$

the nonperturnative and pertubative running agree within $\sim 1\%$ for $X = \gamma_\mu$ and within $\sim 1\%$ for $X = \slashed{q}$.

D. Quark wave function renormalization factor

As for the quark mass, we find that the chiral extrapolations are well under control; they are presented in Appendix C. Here we focus on the scale dependence.

TABLE V.   Running between 2 and 2.5 GeV for the quark wave function in $\overline{\text{MS}}$ and in the SMOM schemes $\gamma_\mu(\omega = 1)$ and $\slashed{q}$. In this case the running is known at NNNLO.

Scheme	LO	NLO	NNLO	NNNLO	NP
$\overline{\text{MS}}$	1.0	1.0048	1.0062	1.0064	
$\overline{\text{MS}} \leftarrow \gamma_\mu$	1.0	1.0069	1.0078	N.A.	
$\overline{\text{MS}} \leftarrow \slashed{q}$	1.0	1.0195	1.0175	1.0146	
γ_μ	1.0	1.0017	1.0020	N.A	1.0037(20)
$\slashed{q}$	1.0	1.0048	1.0081	1.0113	1.0195(25)

---

[5]The attentive reader would have noticed that in Table I the NLO for γ_μ and $\slashed{q}$ are identical. This seems to be nothing but a numerical accident: adding more significant figures leads to 0.941112 for γ_μ and 0.944132 for $\slashed{q}$.

TABLE VI. Study of the convergence of the perturbative series for running of the quark wave function between 2 and 2.5 GeV in $\overline{\text{MS}}$, SMOM-γ_μ, and $\displaystyle{\not{q}}$.

Scheme	NLO-LO	NNLO-NLO	NNNLO-NNLO
$\overline{\text{MS}}$	0.0048	0.0013	0.0003
γ_μ	0.0017	0.0003	
$\not{q}$	0.0048	0.0033	0.0032

Our results are shown for $\omega = \omega_0$: in Figs. 10 and 11 we compare the nonperturbative running to the perturbative prediction. Then in Figs. 12 and 13 we again fix $\omega_0 = 2$ and $\mu_0 = 2.5$ GeV as reference points and let ω and μ vary. Here the situation is very different from the quark mass, mainly because there is no contribution at leading order (in the Landau gauge). A numerical study of the convergence can be found in Tables V and VI. In the $\not{q}$ scheme, the
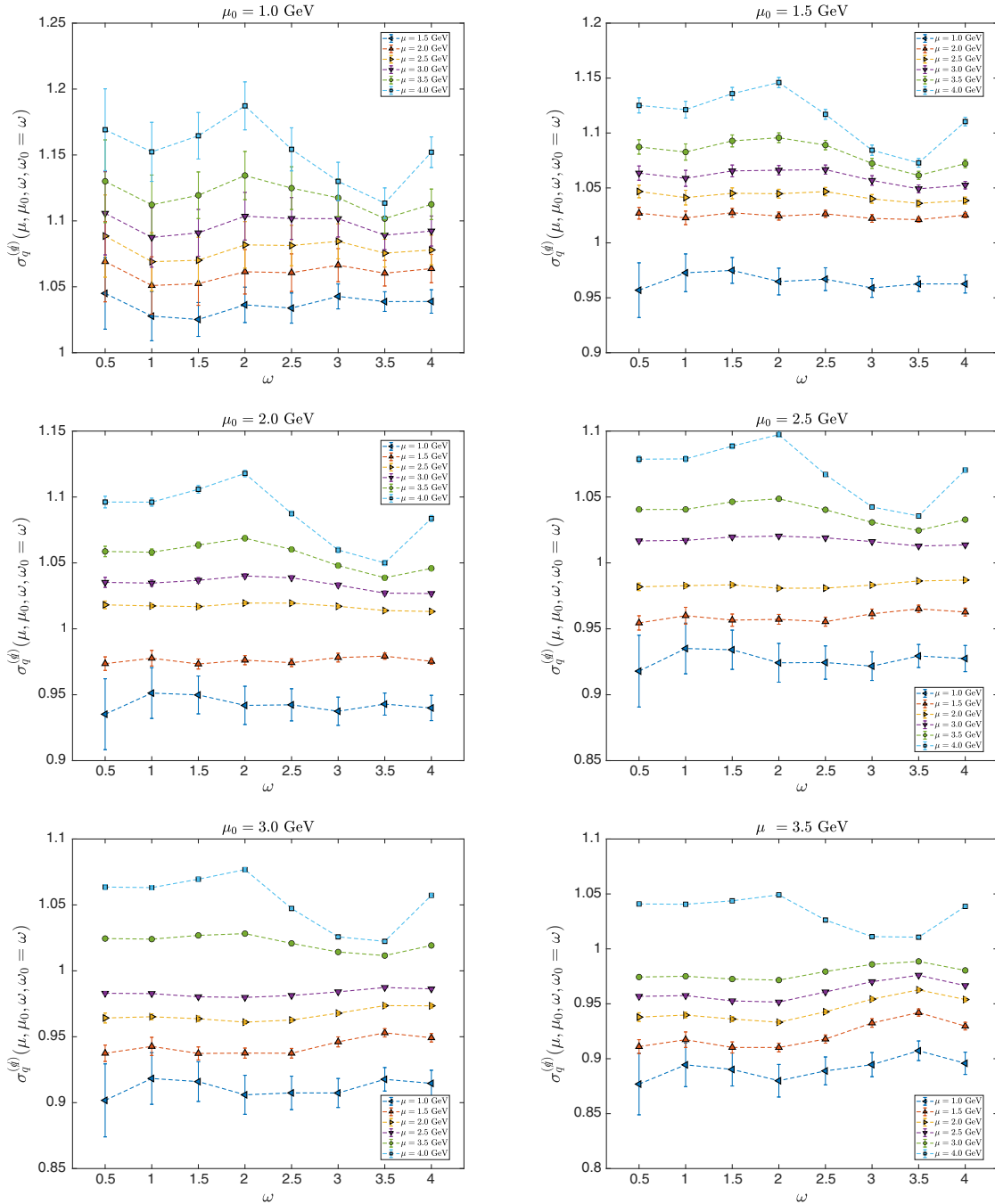

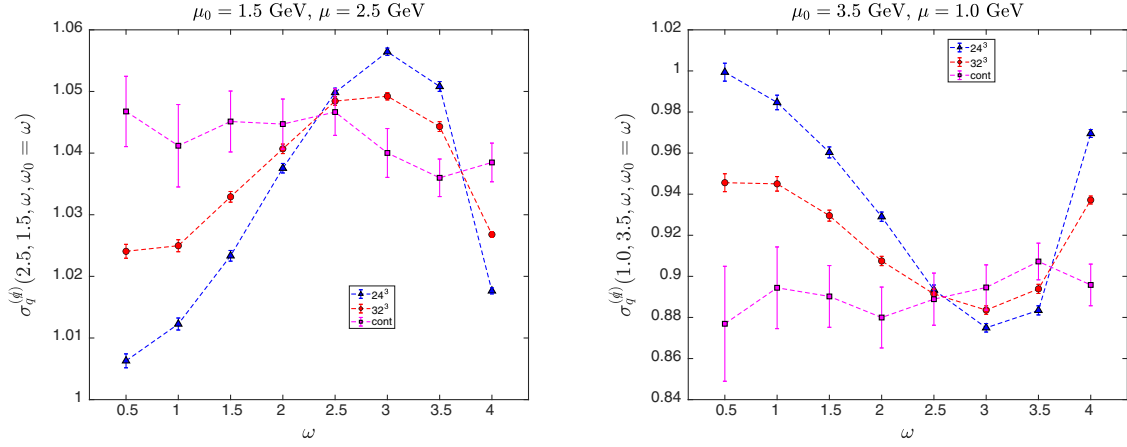FIG. 14. $\sigma_q^{(\not{q})}(\mu, \mu_0, \omega, \omega_0)$ for $\omega_0 = \omega$, statistical error only.

FIG. 15. Example of continuum extrapolations for $\sigma_q^{(q)}(\mu, \mu_0, \omega, \omega_0)$.

nonperturbative results differ significantly from the perturbative predictions; however, one should keep in mind that the running is very small in magnitude. It is also interesting to have a close look at the $\not{q}$ scheme where there the perturbative prediction is known at N³LO. As we can see, the perturbative series seems to converge very poorly in the sense that the relative difference decreases very slowly as we increase the order of the expansion. Therefore we conclude that the difference between the nonperturbative result and the N³LO, namely ~$1.0195 - 1.0113 \sim 0.0082$, could be explained by higher order in the perturbative series.

E. Study of the ω (in)dependence of σ_q

Due to the vector WTI given in Eq. (3.16), we might expect $Z_q^{(q)}$ to be ω independent up to lattice artifacts. This is illustrated in Fig. 14 where we show $\sigma_m^{(q)}(\mu, \mu_0, \omega, \omega_0)$ as a function of $\omega = \omega_0$ for different values of μ and μ_0. We can see that this property is rather well satisfied as long as the scales remain moderate, say $\mu, \mu_0 \leq 3$ GeV. However it is worth noting that this invariance is only true in the continuum, as can be seen in Fig. 15. At finite lattice spacing, within our small statistical errors, the

lattice artifacts are visible and $Z_q^{(q)}$ clearly shows a ω dependence. These figures also suggest that the lattice artifacts are well under control, with two lattice spacings, as long as we do not go too high in energy. Note that in these plots, the systematic errors due to the continuum extrapolations are not included. The nonperturbative-scale evolution of Z_q, $\sigma_q(\mu, \mu_0)$ with $\mu_0 = 2$ GeV and $\omega = \omega_0$ for various values of μ and ω can be found in Tables VII and VIII.

Also it is interesting to notice in Fig. 15 how the discretization effects depend on ω. Clearly for $\omega = 2.0$ and 2.5 the lattice artifacts are much smaller than for $\omega = 1.0$. Of course this effect is quantity dependent but such a property could be very useful in future computations.

F. Study of the chiral symmetry breaking effects

One of the original arguments to motivate the RI/SMOM schemes is a drastic reduction of the systematics errors due to spontaneous chiral symmetry breaking. Even though these effects are physical, they can prevent a clean determination of the renormalization factors because they are absent from the perturbative calculations. This is particularly true for quantities like

TABLE VII. Nonperturbative running for the quark wave function in the γ_μ scheme.

$\omega/\mu =$	1.0	1.5	2.5	3.0	3.5	4.0
0.5	0.972(8)	0.993(4)	1.008(4)	1.014(8)	1.023(14)	1.040(26)
1.0	0.976(8)	0.994(3)	1.004(2)	1.007(5)	1.012(8)	1.021(15)
1.5	0.978(4)	0.998(2)	1.003(1)	1.005(2)	1.006(3)	1.004(3)
2.0	0.990(7)	0.998(2)	1.003(0)	1.005(1)	1.007(1)	1.008(1)
2.5	0.987(5)	0.997(2)	1.001(1)	1.002(2)	1.002(3)	1.003(4)
3.0	0.985(4)	0.999(2)	1.000(2)	0.998(4)	0.993(9)	0.978(18)
3.5	0.989(5)	1.001(2)	0.997(2)	0.993(6)	0.982(13)	0.959(27)
4.0	0.990(5)	0.999(1)	0.994(3)	0.983(8)	0.957(22)	0.887(60)

TABLE VIII.   Nonperturbative running for the quark wave function in $\slashed{q}$ scheme. Here we expect the results to be ω independent.

$\omega/\mu =$	1.0	1.5	2.5	3.0	3.5	4.0
0.5	0.935(27)	0.974(7)	1.018(7)	1.035(16)	1.059(31)	1.096(56)
1.0	0.951(19)	0.978(6)	1.017(6)	1.035(14)	1.058(28)	1.096(51)
1.5	0.950(15)	0.973(4)	1.017(4)	1.037(11)	1.064(25)	1.106(49)
2.0	0.942(15)	0.976(3)	1.020(3)	1.040(8)	1.069(20)	1.118(45)
2.5	0.942(14)	0.974(3)	1.019(1)	1.039(3)	1.060(9)	1.087(20)
3.0	0.937(12)	0.978(4)	1.017(2)	1.033(2)	1.048(2)	1.060(2)
3.5	0.943(10)	0.979(3)	1.014(2)	1.027(3)	1.039(3)	1.050(2)
4.0	0.940(10)	0.975(4)	1.013(3)	1.027(8)	1.046(18)	1.084(40)

Π_P and Σ^S where the presence of pseudo-Goldstone poles can completely dominate the signal. In practice, the vertex functions from which we want to extract the Z factors are "polluted" by negative powers of the quark mass or the momentum scale. Of course these chiral symmetry breaking effects are nonperturbative and disappear for high momentum. However, we want to keep the Rome-Southampton windows as open as possible, so it is always desirable to reduce this infrared contamination or, at least, keeping them well under control.

If chiral symmetry is exactly realized then we should find that $Z_S = S_P$ and $Z_V = Z_A$. Therefore, in order to study these chiral symmetry breaking affects as a function of ω, we study the deviation of Z_V from Z_A and Z_S from Z_P. We start by the analysis of the ratio Z_V/Z_A, see Fig. 16 for $\omega = 1$ using the γ_μ projector. In the left panel, we show our results for the various quark masses as a function of μ. On the right panel, we show the chiral extrapolation for $\omega = 1$ and $\mu = 1$ GeV. There we

observe a deviation from one at the order of a few percents (the reader would notice that this is one of the worst-case scenarios). However we do not see any pole in powers of $1/m$. We find the quark mass dependence to be linear within our statistical error; therefore, we extrapolate to the chiral limit using a straight line. In Fig. 17 we observe that—as expected—the ratio Z_V/Z_A collapses quickly to one as the energy scale increases: at $\mu = 2$ GeV, the deviation from one is at most at the per-mille level. Our results for the $\slashed{q}$ projector are very similar. Our results seem to indicate a trend that Z_V/Z_A increases toward one when ω increases between 0.5 and 2 ($Z_V/Z_A \sim 0.98$ at $\omega = 1$ and $Z_V/Z_A \sim 0.99$ at $\omega = 2$), but this could well be a statistical effect. Altogether we find that $Z_V/Z_A = 1$ to a very good approximation for all values of ω. This is true for both values of the lattice spacing and both projectors $X \in (\gamma_\mu, \slashed{q})$.

We also study $(\Lambda_S - \Lambda_P)/\Lambda_V$, which is proportional to $Z_V(1/Z_S - 1/Z_P)$. Our results are shown in Fig. 18.
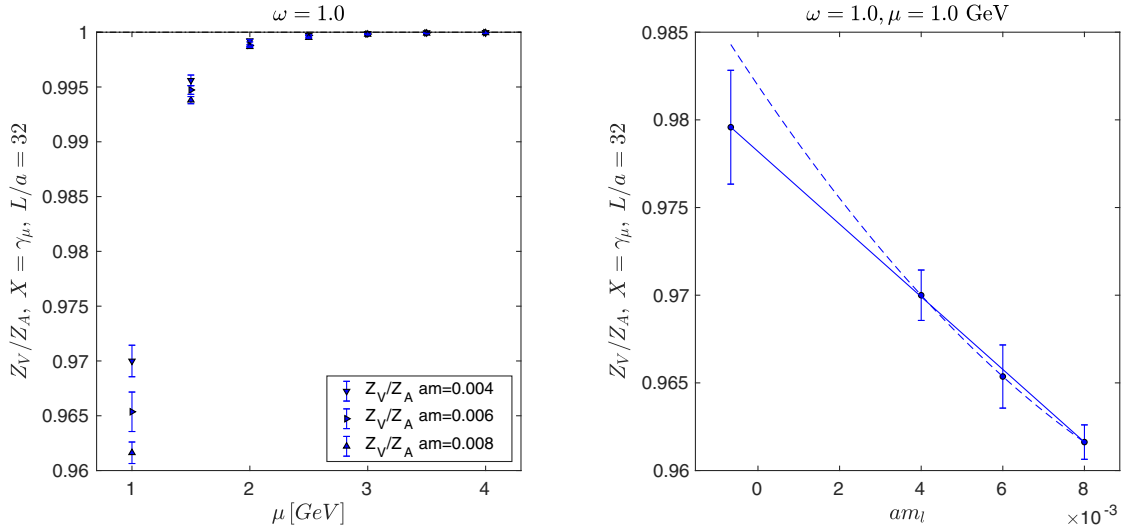
FIG. 16. Z_V/Z_A for the γ_μ projector as a function of μ for $\omega = 1$. In the left panel we show the results at finite quark masses as a function of the energy scale. As an example of chiral extrapolations, in the right panel we show our results for $\mu = 1$ GeV, $\omega = 1$. We perform a linear extrapolation (solid line), and a quadratic extrapolation is shown as a dashed line for illustration.
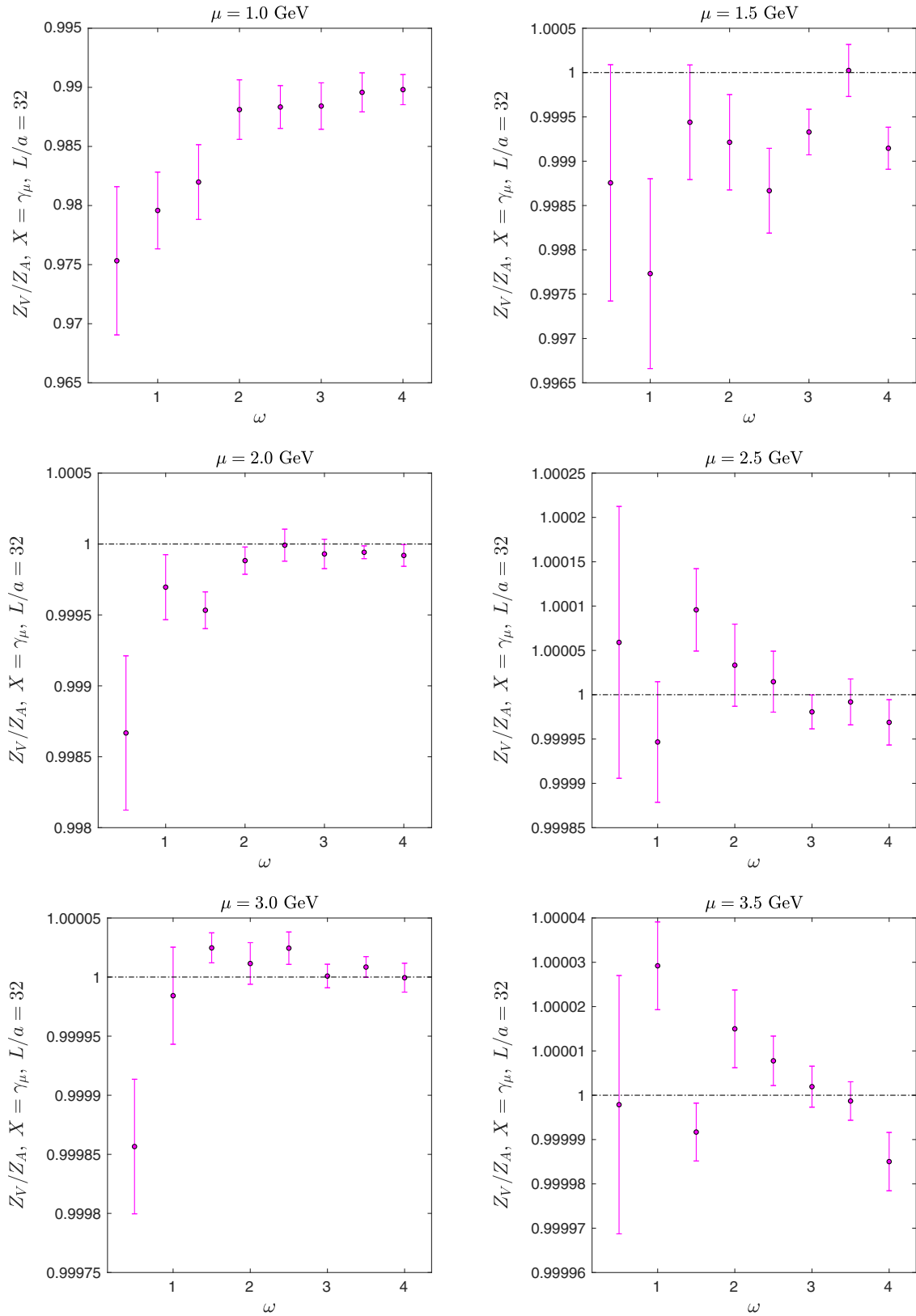
FIG. 17. Z_V/Z_A for the γ_μ projector as a function of ω for various values of μ.

Here it is clear that the infrared effects due to chiral symmetry breaking decrease when the value of ω increases. For example, we observe that at $\mu = 1.5$ GeV, $(\Lambda_S - \Lambda_P)/\Lambda_V \sim 0.1$. The same quantity reduces to ~ 0.03 for $\omega = 2.0$. For illustration, we show Z_S/Z_V and Z_P/Z_V

versus μ for the different quark masses in Fig. 19. It will be interesting to perform a similar study on four-quark operators, especially those where the infrared contamination can be important and a source of disagreement (see for example the section on BSM kaon mixing in FLAG [24,8]).
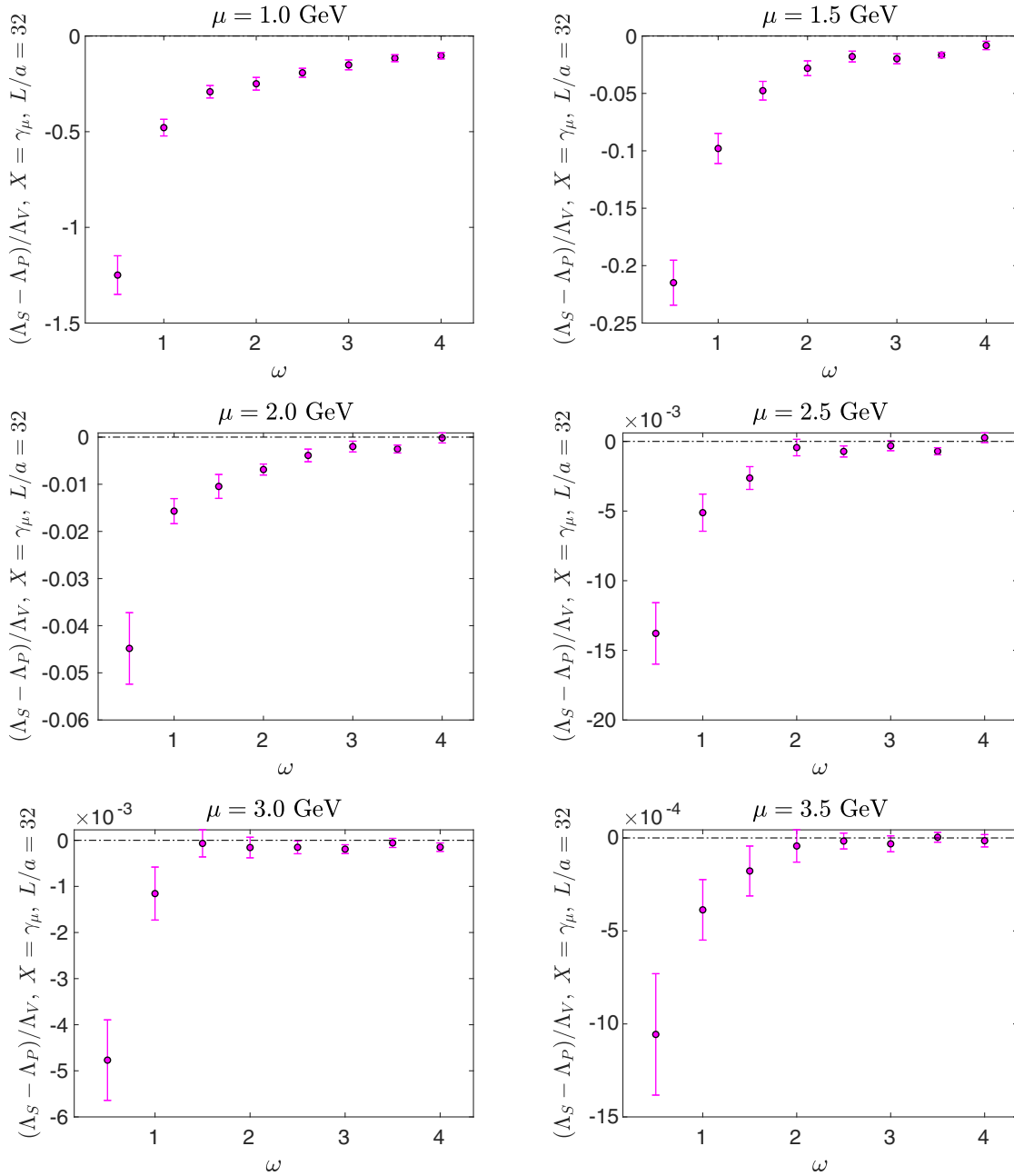

FIG. 18. $(\Lambda_S - \Lambda_P)/\Lambda_V$ for the γ_μ projector as a function of ω for various values of μ.
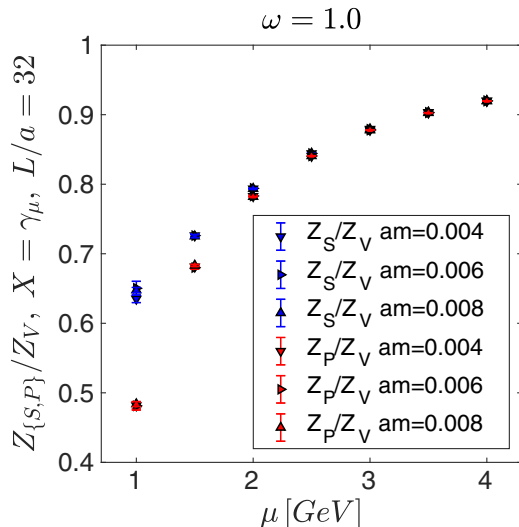
FIG. 19. Z_S and Z_P at finite quark masses versus the renormalization scale for $\omega = 1$.

(i) significantly smaller contributions of the pseudo-Goldstone poles contamination in $\Lambda_P - \Lambda_S$,

(ii) reduction of the discretization effects in the vector WTI.

We remind the reader that $\omega = 2$ corresponds to an angle $\alpha = \pi/2$ between the incoming and outgoing momenta, see Fig. 2. With our choice of kinematics, this means that p_1 and p_2 are parallel to the x axis and y axis, respectively. Therefore this choice of kinematics takes advantage of the hypercubic symmetry of the lattice. In addition, any term proportional to $p_1.p_2$ is also absent in this setup. Therefore we believe that the improvements that we observe for are not accidental but genuinely come from the kinematics. Of course this statement needs to be checked on different quantities. It will be interesting to extend this study to the case of four-quark operators where the infrared contaminations due to chiral symmetry breaking are significantly more sizeable, and one of the dominant sources of systematic errors.

V. CONCLUSIONS AND OUTLOOK

As a proof of concept we have implemented several IMOM schemes defined via two different projectors for various values of the kinematics parameter ω. In this framework we have determined the renormalization factors and nonperturbative scale evolution functions of the quark mass and of the quark wave function. To compare our lattice results with NNLO results in continuum perturbation theory, we also present the numerical form of the perturbative scheme conversion factors for these schemes in these general kinematics.

We find that the nonpertubative and perturbative results agree very well as long as we stay away from the corner of the (ω, μ) plane, with one exception, namely $Z_q^{(\slashed{q})}$. For the quark wave function renormalization, we argued that the reason for the relatively bad agreement is the poor convergence of the perturbative expansion. Clearly, having several values of ω helps to have a better handle on the systematic errors coming from the NPR procedure. As an application, we have seen a example where the discretization effects depend significantly on ω (see $\sigma_q^{(\slashed{q})}$ where the discretization effects for $\omega = 2, 2.5$ are much smaller than for $\omega = 1$), and so does the perturbative convergence. In this proof of concept study, only two lattice spacings have been used. Clearly, adding a finer lattice could potentially allow us to test the agreement of the perturbative and nonperturbative window even further.

Generally speaking, it is well known that the SMOM kinematics ($\omega = 1$) leads to much cleaner determinations of the renormalization factors than the $\omega = 0$ case. In this work, we have shown that increasing the value of ω to $\omega \sim 2$ has the potential to improve these determinations even further:

APPENDIX A: PERTURBATION THEORY

In order to make contact to phenomenology, results obtained from lattice simulations need to be converted to a scheme that is used in continuum perturbation theory such as $\overline{\text{MS}}$. The nonperturbative renormalization schemes used in this work serve as an intermediate scheme that can be defined on the lattice and in the continuum. This enables us to compare the nonperturbative with the perturbative change of the renormalization scheme parameters μ and ω. This appendix provides the ingredients for the perturbative scheme changes at NNLO.

TABLE IX. Values of the strong running coupling as a function of the dimensional regularization scheme ν. They are obtained in the $\overline{\text{MS}}$ scheme in the three-flavor theory.

ν/GeV	1.0	1.5	2.0	2.5	3.0	3.5	4.0
$\alpha_S(\nu)$	0.4698	0.3467	0.2950	0.2652	0.2452	0.2307	0.2196

The dependence of the strong coupling constant on the dimensional regularization scale ν in the $\overline{\text{MS}}$ scheme is governed by the β function

$$\nu^2 \frac{d}{d\nu^2}\left(\frac{\alpha_s}{4\pi}\right) \equiv -\sum_{i=0}^{\infty} \beta_i \left(\frac{\alpha_s}{4\pi}\right)^{i+2}. \qquad (A1)$$

Although it is known at five loops [25–27], we will only use the first three coefficients in the expansion to be consistent with our NNLO analysis of the running. In the following we will need the first two coefficients,

$$\beta_0 = 11 - \frac{2}{3}N_f, \qquad (A2)$$

$$\beta_1 = 102 - \frac{38}{3}N_f, \qquad (A3)$$

where we fixed the number of colors $N_c = 3$ in this and the following expressions. Using $\alpha_S(M_Z) = 0.1179(10)$ and $M_Z = 91.1876(21)$ GeV [28] we find the required values of the strong coupling constant for $N_f = 3$ flavors given in Table IX. To arrive at three active flavors, we decoupled the bottom and charm quark at $\nu_b = 5$ GeV and $\nu_c = 1.5$ GeV respectively using central values $m_b(m_b) = 4.13$ GeV and $m_c(m_c) = 1.27$ GeV for the quark masses in the $\overline{\text{MS}}$ scheme [28]. The relevant threshold effects and running of the strong coupling constant are implemented using RunDec [29].

The fields and masses in the $\text{IMOM}^{(X)}$ schemes are related to the $\overline{\text{MS}}$ scheme as $\psi_{\overline{\text{MS}}}(\nu) = (Z_q^{\overline{\text{MS}}}/Z_q^{(X)})\psi_X(\mu,\omega)$ and $m^{\overline{\text{MS}}}(\nu) = (Z_m^{\overline{\text{MS}}}/Z_m^{(X)})m_X(\mu,\omega)$, where $X \in (\gamma_\mu, \slashed{q})$. The continuum perturbation theory expansion of the conversion factors

$$\frac{Z_i^{\overline{\text{MS}}}(\epsilon,\nu)}{Z_i^{(X)}(\epsilon,\mu,\omega)} \overset{\epsilon \to 0}{=} C_i^{(X)}(\nu,\mu,\omega), \qquad i \in \{q,m\} \qquad (A4)$$

are known up to two loops [10,20] for the IMOM scheme and up to three loops [13,14] in the SMOM limit, i.e. where $\omega = 1$. Writing

$$C_i^{(X)} = 1 + \frac{\alpha_s}{4\pi}C_i^{(X,1)} + \frac{\alpha_s^2}{(4\pi)^2}C_i^{(X,2)} \qquad (A5)$$

TABLE X. The perturbative expansion coefficients of the conversion factors $C_m^{(\gamma)}$, $C_m^{(\slashed{q})}$, $C_q^{(\gamma)}$, and $C_q^{(\slashed{q})}$ as a function of ω. Note that $C_q^{(\slashed{q})}$ is independent of ω.

ω	$C_m^{(\slashed{q},1)}$	$C_m^{(\slashed{q},2)}$	$C_m^{(\gamma,1)}$	$C_m^{(\gamma,2)}$
0.5	-2.422	$-64.756 + 5.988N_f$	-3.248	$-89.07 + 7.571N_f$
1.0	-0.646	$-22.608 + 4.014N_f$	-1.979	$-55.032 + 6.162N_f$
1.5	0.778	$10.344 + 2.432N_f$	-0.964	$-28.916 + 5.035N_f$
2.0	1.994	$38.567 + 1.08N_f$	-0.098	$-6.829 + 4.072N_f$
2.5	3.071	$63.81 - 0.115N_f$	0.667	$12.741 + 3.222N_f$
3.0	4.042	$86.961 - 1.195N_f$	1.358	$30.56 + 2.454N_f$
3.5	4.933	$108.544 - 2.184N_f$	1.99	$47.076 + 1.752N_f$
4.0	5.757	$128.894 - 3.1N_f$	2.575	$62.576 + 1.102N_f$

ω	$C_q^{(\slashed{q},1)}$	$C_q^{(\slashed{q},2)}$	$C_q^{(\gamma,1)}$	$C_q^{(\gamma,2)}$
0.5	0	$-25.464 + 2.333N_f$	0.825	$1.53 + 0.75N_f$
1.0	0	$-25.464 + 2.333N_f$	1.333	$9.599 + 0.185N_f$
1.5	0	$-25.464 + 2.333N_f$	1.742	$15.476 - 0.269N_f$
2.0	0	$-25.464 + 2.333N_f$	2.093	$20.137 - 0.658N_f$
2.5	0	$-25.464 + 2.333N_f$	2.403	$24.001 - 1.004N_f$
3.0	0	$-25.464 + 2.333N_f$	2.684	$27.292 - 1.316N_f$
3.5	0	$-25.464 + 2.333N_f$	2.942	$30.147 - 1.603N_f$
4.0	0	$-25.464 + 2.333N_f$	3.182	$32.66 - 1.869N_f$

and setting $\mu = \nu$ we find the numerical conversion factors as a function of ω given in Table X. The scheme transformation can then be written as a product

$$U_i^{(X)}(\mu_1,\mu_0,\omega_1,\omega_0) = C_i^{(X)}(\nu_1,\mu_1,\omega_1)U_i^{\overline{\text{MS}}}(\nu_1,\nu_0)$$
$$\times C_i^{(X)^{-1}}(\nu_0,\mu_0,\omega_0)\Big|_{\substack{\mu_0=\nu_0 \\ \mu_1=\nu_1}} \qquad (A6)$$

of the conversion factor, its inverse, and the $\overline{\text{MS}}$ evolution kernel $U_i^{\overline{\text{MS}}}(\nu_1,\nu_0)$. The evolution Kernel fulfils the renormalization group equation

$$\nu^2 \frac{d}{d\nu^2} U_i^{\overline{\text{MS}}}(\nu,\nu_0) = -\gamma_i^{\overline{\text{MS}}} U_i^{\overline{\text{MS}}}(\nu,\nu_0) \qquad (A7)$$

and we expand the anomalous dimensions

$$\gamma_i^{(X)} \equiv \sum_{k=0}^{\infty} \gamma_i^{(X,k)}\left(\frac{\alpha_s}{4\pi}\right)^{k+1}, \qquad (A8)$$

where X denotes the renormalization scheme. Hence we can transform for example a light quark mass renormalized in given scheme X at different kinematic points (μ_1,ω_1) and (μ_0,ω_0) via

$$m^{(X)}(\mu_1,\omega_1) = U_m^{(X)}(\mu_1,\mu_0,\omega_1,\omega_0)m^{(X)}(\mu_0,\omega_0), \qquad (A9)$$

where the logarithms $\log \mu_1/\mu_0$ are summed using renormalization group improved perturbation theory. Explicitly, we find at NNLO

$$U_i^{(X)}(\mu_1,\mu_0,\omega_1,\omega_0) = \left(1 + \frac{\alpha_s(\mu_1)}{4\pi}J_i^{(X,1)}(\omega_1) + \frac{\alpha_s^2(\mu_1)}{(4\pi)^2}J_i^{(X,2)}(\omega_1)\right)\left(\frac{\alpha_s(\mu_0)}{\alpha_s(\mu_1)}\right)^{\gamma_i^{(0)}/\beta_0}$$

$$\times\left(1 - \frac{\alpha_s(\mu_0)}{4\pi}J_i^{(X,1)}(\omega_0) + \frac{\alpha_s^2(\mu_0)}{(4\pi)^2}\left[\left(J_i^{(X,1)}(\omega_0)\right)^2 - J_i^{(X,2)}(\omega_0)\right]\right),$$

TABLE XI. The NLO and NNLO coefficients of anomalous dimensions $\gamma_m^{(\phi)}$, $\gamma_m^{(\gamma)}$, $\gamma_q^{(\gamma)}$, $\gamma_q^{(\phi)}$ as a function of ω. Note that $\gamma_q^{(\phi)}$ is independent of ω.

ω	$\gamma_m^{(\phi,1)}$	$\gamma_m^{(\phi,2)}$
0.5	$93.981 - 3.837 N_f$	$2985.27 - 398.857 N_f + 6.256 N_f^2$
1.0	$74.434 - 2.653 N_f$	$1816.8 - 273.08 N_f + 3.623 N_f^2$
1.5	$58.78 - 1.704 N_f$	$948.781 - 176.459 N_f + 1.515 N_f^2$
2.0	$45.395 - 0.893 N_f$	$240.849 - 95.917 N_f - 0.288 N_f^2$
2.5	$33.558 - 0.175 N_f$	$-364.298 - 25.958 N_f - 1.882 N_f^2$
3.0	$22.868 + 0.473 N_f$	$-896.718 + 36.367 N_f - 3.322 N_f^2$
3.5	$13.075 + 1.066 N_f$	$-1374.46 + 92.858 N_f - 4.641 N_f^2$
4.0	$4.006 + 1.616 N_f$	$-1809.31 + 144.71 N_f - 5.862 N_f^2$

ω	$\gamma_m^{(\gamma,1)}$	$\gamma_m^{(\gamma,2)}$
0.5	$103.057 - 4.387 N_f$	$3655.83 - 479.684 N_f + 8.367 N_f^2$
1.0	$89.101 - 3.541 N_f$	$2704.63 - 382.794 N_f + 6.487 N_f^2$
1.5	$77.943 - 2.865 N_f$	$1993.76 - 308.337 N_f + 4.984 N_f^2$
2.0	$68.413 - 2.288 N_f$	$1409.35 - 246.123 N_f + 3.701 N_f^2$
2.5	$59.993 - 1.777 N_f$	$905.536 - 191.915 N_f + 2.567 N_f^2$
3.0	$52.396 - 1.317 N_f$	$458.454 - 143.458 N_f + 1.544 N_f^2$
3.5	$45.441 - 0.895 N_f$	$53.89 - 99.383 N_f + 0.607 N_f^2$
4.0	$39.005 - 0.505 N_f$	$-317.4 - 58.784 N_f - 0.26 N_f^2$

ω	$\gamma_q^{(\gamma,1)}$	$\gamma_q^{(\gamma,2)}$
0.5	$13.257 - 0.783 N_f$	$417.983 - 65.569 N_f + 1.741 N_f^2$
1.0	$7.667 - 0.444 N_f$	$200.702 - 36.683 N_f + 0.988 N_f^2$
1.5	$3.171 - 0.172 N_f$	$43.556 - 14.519 N_f + 0.382 N_f^2$
2.0	$-0.684 + 0.062 N_f$	$-79.969 + 3.809 N_f - 0.137 N_f^2$
2.5	$-4.102 + 0.269 N_f$	$-181.296 + 19.56 N_f - 0.597 N_f^2$
3.0	$-7.195 + 0.456 N_f$	$-266.635 + 33.428 N_f - 1.014 N_f^2$
3.5	$-10.033 + 0.628 N_f$	$-339.81 + 45.844 N_f - 1.396 N_f^2$
4.0	$-12.666 + 0.788 N_f$	$-403.372 + 57.097 N_f - 1.751 N_f^2$

ω	$\gamma_q^{(\phi,1)}$	$\gamma_q^{(\phi,2)}$
0…4	$22.333 - 1.333 N_f$	$1088.54 - 146.397 N_f + 3.852 N_f^2$

where the $J_X^{(1)}$ and $J_X^{(2)}$ are given by

$$J_i^{(X,1)} = \frac{\gamma_i^{(X,1)}}{\beta_0} - \frac{\beta_1\gamma_i^{(0)}}{\beta_0^2},$$

$$J_i^{(X,2)} = \frac{1}{2}\left(J^{(X,1)2} + \frac{\gamma_i^{(X,2)}}{\beta_0} + \frac{\beta_1^2\gamma_i^{(0)}}{\beta_0^3} - \frac{\beta_1\gamma_i^{(X,1)}}{\beta_0^2} - \frac{\beta_2\gamma_i^{(0)}}{\beta_0^2}\right).$$

$$(A10)$$

The leading order anomalous dimensions

$$\gamma_q^{(0)} = 0,$$

$$\gamma_m^{(0)} = 4 \qquad (A11)$$

are scheme independent. The expressions for the NLO and NNLO anomalous dimensions are given in Table XI for different values of ω as a function of the number of flavors N_f.

APPENDIX B: SIMULATION DETAILS

Our numerical work is based on RBC-UKQCD data; the lattice details can be found in [16]. We compute the propagators using Landau gauge-fixed $2 + 1$, domain-wall (Shamir [30])/Iwasaki lattices. The values of the parameters can be found in [7].

In a nutshell, we use two lattice spacings (we refer to them as 24^3 and 32^3):

$$a^{-1} = 1.785(5) \text{ GeV} \quad (24^3), \qquad (B1)$$

$$a^{-1} = 2.383(9) \text{ GeV} \quad (32^3), \qquad (B2)$$

for each lattice spacing we have three different sea quark masses, $am = 0.005, 0.010, 0.020$ for the $24^3 \times 64 \times 16$ lattice and $am = 0.004, 0.006, 0.008$ for the $32^3 \times 64 \times 16$ lattice.

We take the chiral limit on each lattice spacing using the values

$$am_{\text{res}} = 0.003152(43) \quad (24^3), \qquad (B3)$$

$$am_{\text{res}} = 0.0006664(76) \quad (32^3). \tag{B4}$$

Our values for Z_V are [17]

$$Z_V = 0.71651(46) \quad (24^3), \tag{B5}$$

$$Z_V = 0.74475(12) \quad (32^2). \tag{B6}$$

**APPENDIX C: CHIRAL EXTRAPOLATIONS
OF THE Z FACTORS**

In Figs. 20 and 21 we show our chiral extrapolations for Z_m and Z_q at fixed scale $\mu = 2$ GeV and for various ω. Since we use domain-wall fermions, there is small additive mass renormalization; therefore, the chiral limit is situated at
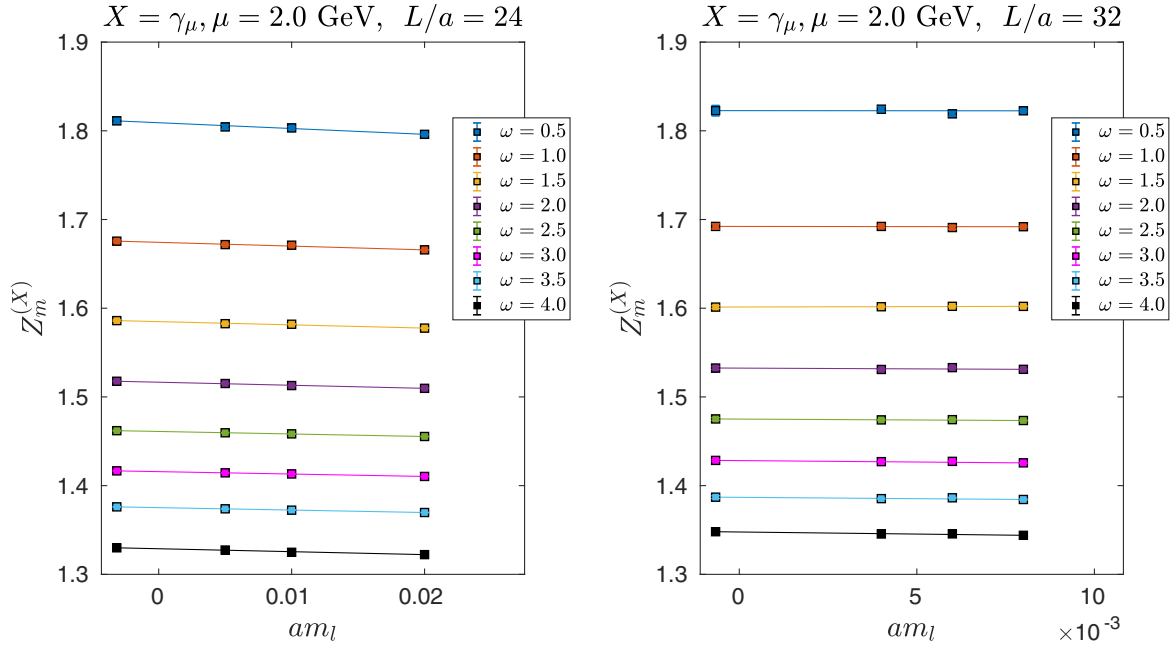
FIG. 20. Chiral extrapolation of Z_m at $\mu = 2$ GeV.
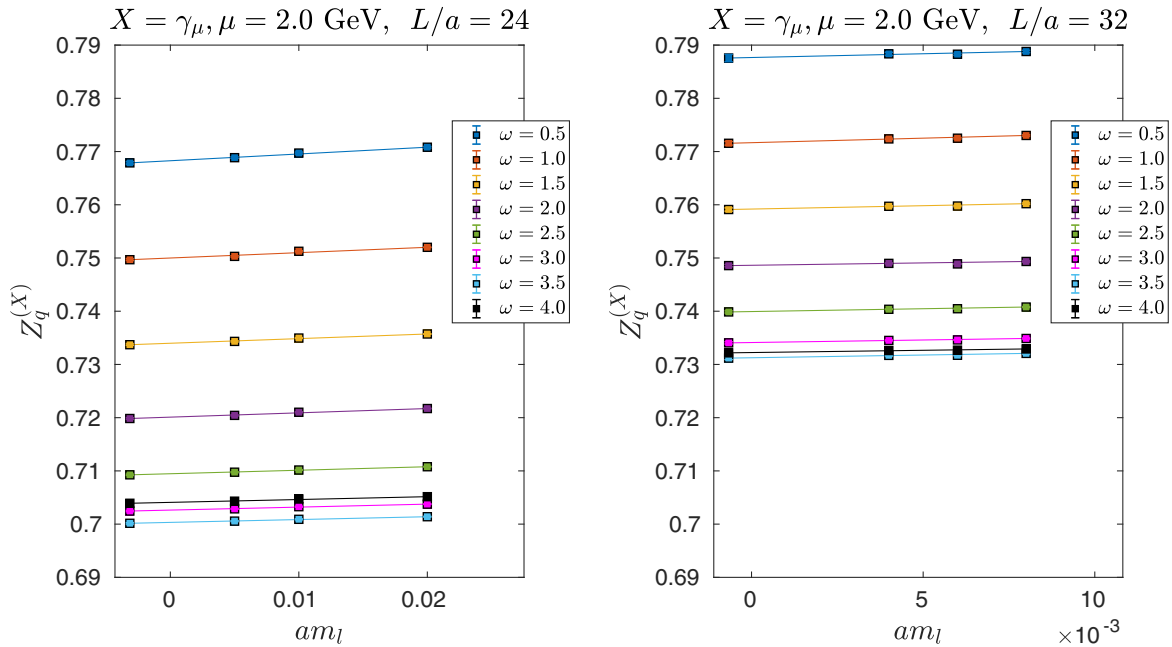
FIG. 21. Chiral extrapolation of Z_q at $\mu = 2$ GeV.

$am_l = -am_{res}$. The values of the residual mass are given in Appendix B. We find a very mild quark mass dependence (if any) and simply perform a linear extrapolation.

APPENDIX D: $Z_m^{(X)}$ FOR $X = \not{q}$

In Figs. 22 and 23 we show the equivalent of Figs. 4 and 5 for $X = \not{q}$ on the $L/a = 32$ lattice. See Sec. IV A for more details.
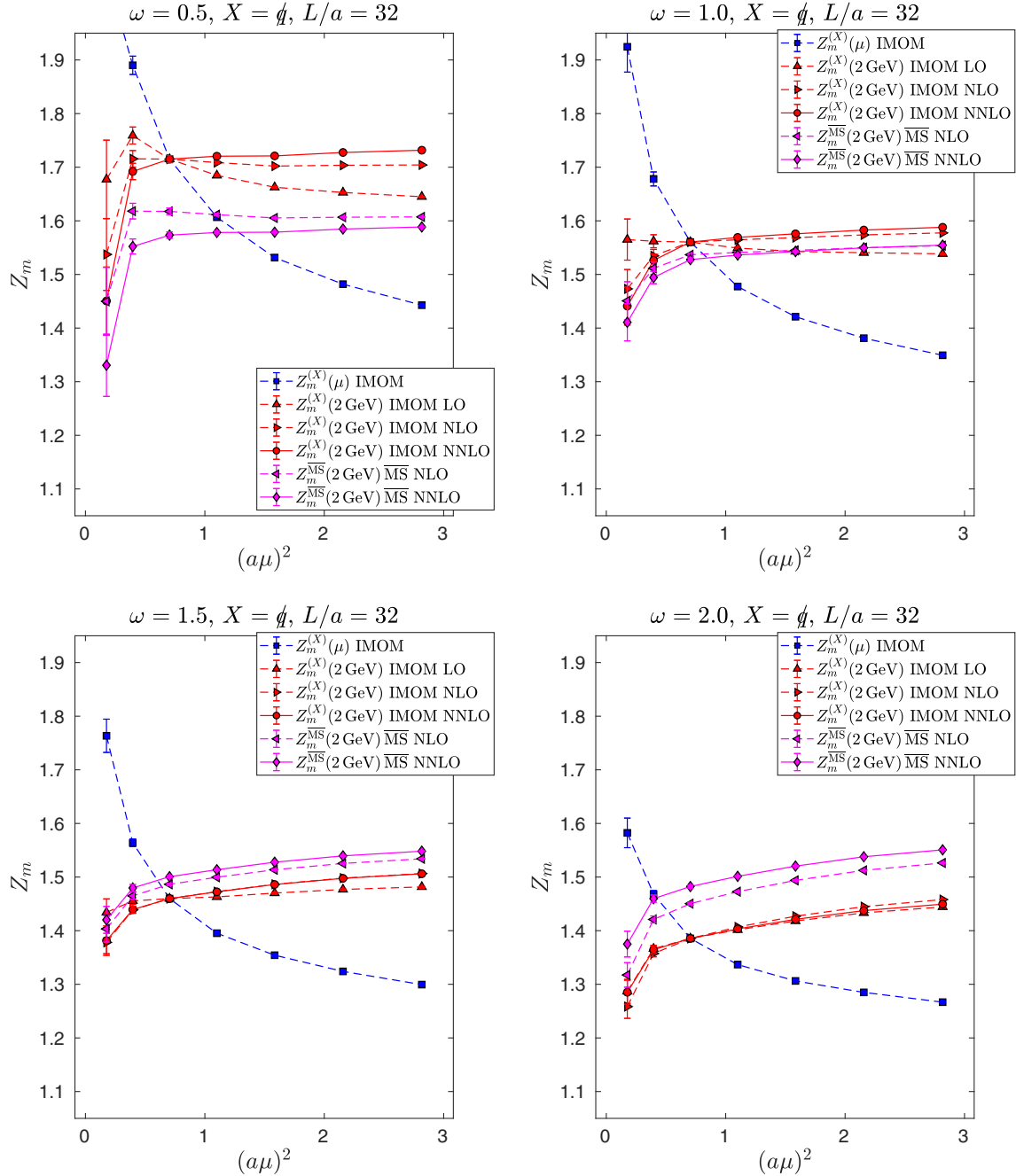
FIG. 22. Z_m at $\mu = 2$ GeV in $\overline{\text{MS}}$ converted from $X = \not{q}$ and for $\omega = 0.5, 1.0, 1.5, 2.0$.
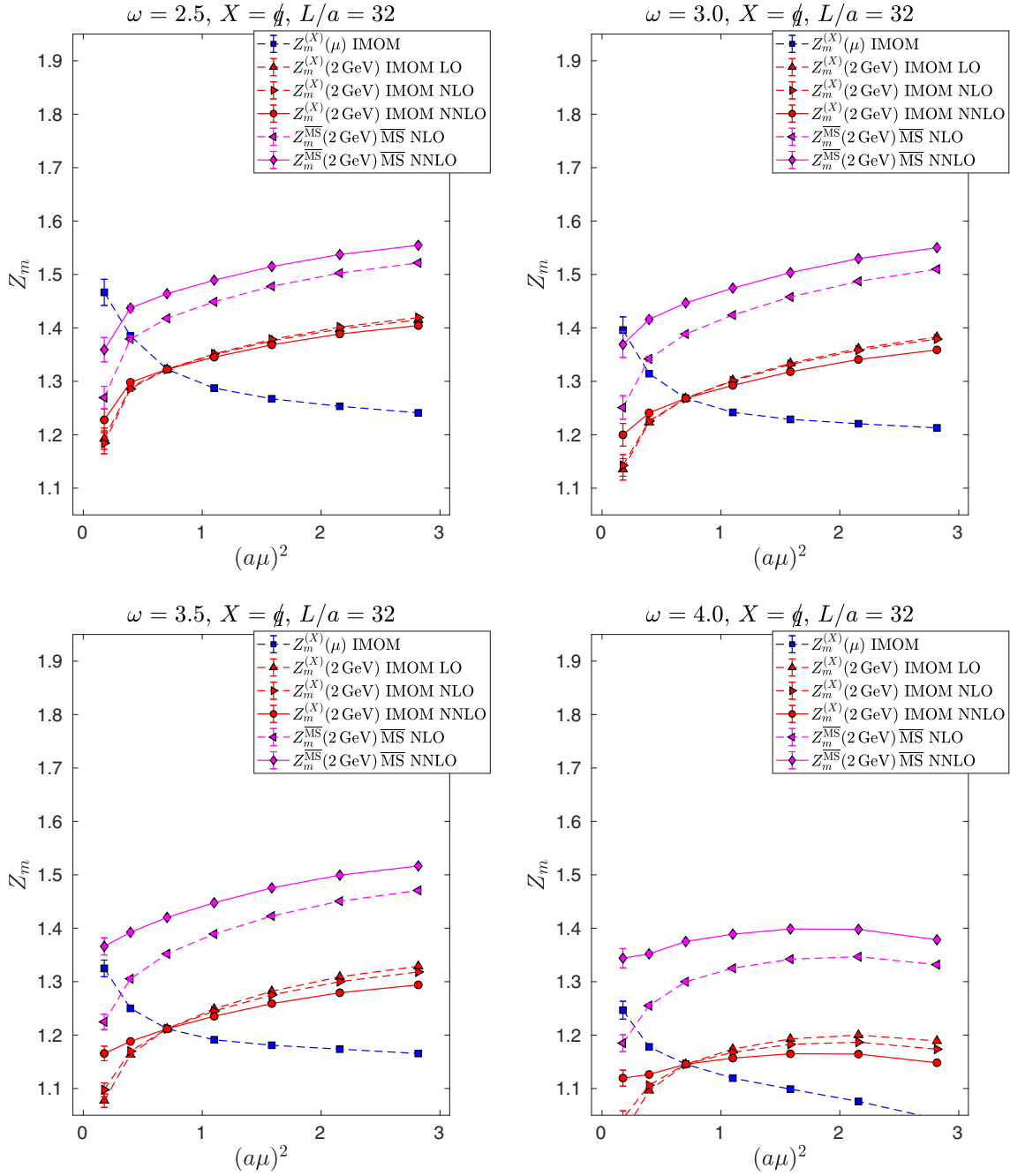
FIG. 23.   Same as Fig. 22 for $\omega = 2.5, 3.0, 3.5, 4.0$.

APPENDIX E: EXTENSIVE STUDY FOR $\sigma_m^{(X)}$

In this appendix we provide our numerical results for running of the quark mass. These results are given for $\sigma_m^{(X)}(\mu, \mu_0, \omega, \omega_0)$ as defined in Eq. (4.5), such that

$$Z_m^{(X)}(\mu, \omega) = \sigma_m^{(X)}(\mu, \mu_0, \omega, \omega_0) Z_m^{(X)}(\mu_0, \omega_0). \quad \text{(E1)}$$

1. Study of the ω dependence for fixed energy scales

In order to study the ω dependence, we first fix μ and μ_0 to some reasonable values, where we expect a rather good control over both the perturbative errors and the lattice artifacts. We choose $(\mu_0, \mu) = (2.5 \text{ GeV}, 1.5 \text{ GeV})$. We then vary ω, but first we only consider the "diagonal" case, i.e. $\omega_0 = \omega$. We show our results in

TABLE XII. Running for the quark mass, γ_μ scheme for $(\mu_0, \mu) = (2.5 \text{ GeV}, 1.5 \text{ GeV})$.

$(\mu_0,\mu) = (2.5, 1.5)$ $\omega = \omega_0 \downarrow$	$\sigma_m^{(\gamma_\mu)}$	σ_m/LO	σ_m/NLO	$\sigma_m/NNLO$
0.5	1.229(27)	1.091(24)	1.035(23)	1.006(22)
1.0	1.174(18)	1.042(16)	0.999(16)	0.984(15)
1.5	1.184(17)	1.051(15)	1.016(15)	1.009(15)
2.0	1.162(16)	1.032(14)	1.005(14)	1.004(14)
2.5	1.143(14)	1.014(12)	0.994(12)	0.998(12)
3.0	1.124(12)	0.998(11)	0.982(11)	0.990(11)
3.5	1.110(11)	0.985(9)	0.975(9)	0.986(9)
4.0	1.080(5)	0.959(5)	0.952(5)	0.967(5)

TABLE XIII. Same as Table XII.

$(\mu_0,\mu) = (2.5, 1.5)$ $\omega = \omega_0 \downarrow$	$\sigma_m^{(\not{q})}$	σ_m/LO	σ_m/NLO	$\sigma_m/NNLO$
0.5	1.194(23)	1.059(21)	1.012(20)	0.992(20)
1.0	1.138(18)	1.010(16)	0.980(16)	0.995(16)
1.5	1.138(13)	1.010(11)	0.991(11)	0.985(11)
2.0	1.117(13)	0.992(12)	0.981(12)	1.000(12)
2.5	1.096(13)	0.973(11)	0.970(11)	0.971(11)
3.0	1.080(13)	0.959(12)	0.962(12)	0.984(12)
3.5	1.068(11)	0.948(9)	0.956(10)	0.963(10)
4.0	1.033(12)	0.917(10)	0.929(10)	0.952(11)

Tables XII and XIII. The middle column shows the running itself obtained from the lattice, while the other three columns on the right show the ratio of the non-perberturbative running over the perturbative prediction at leading order (LO), next-to-leading order (NLO), and next-to-next-to-leading order (NNLO). The errors quoted there combine an estimate of the discretization errors and the statistical one.

We observe that the nonperturbative running agrees extremely well with NNLO predictions for all values of $0.5 \leq \omega \leq 3$. Looking at the perturbative convergence and stability, our data seem to favor the region $\omega \sim 2$.

2. Study of the ω dependence for larger energy ranges

Here we fix $\mu = 2$ GeV and let μ_0 vary over the full range. Again we only consider the case $\omega_0 = \omega$. The rows

TABLE XIV. Running for the quark mass, $X = \gamma_\mu, \mu = 2$ GeV. We only consider $\omega = \omega_0$ and let μ_0 vary between 1 and 4 GeV.

$\mu_0 \downarrow$ (GeV)	σ_m	σ_m/LO	σ_m/NLO	$\sigma_m/NNLO$
$\omega = 0.5$				
1.0	0.826(83)	1.015(102)	1.145(115)	1.246(126)
1.5	0.884(17)	0.949(19)	0.982(19)	1.001(20)
2.0	1	1	1	1
2.5	1.084(10)	1.034(9)	1.014(9)	1.005(9)
3.0	1.153(17)	1.062(15)	1.029(15)	1.014(15)
3.5	1.206(24)	1.081(22)	1.038(21)	1.019(21)
4.0	1.253(35)	1.099(31)	1.048(30)	1.027(29)
$\omega = 1.0$				
1.0	0.740(42)	0.910(51)	0.999(56)	1.045(59)
1.5	0.916(13)	0.984(14)	1.010(15)	1.021(15)
2.0	1	1	1	1
2.5	1.074(7)	1.025(7)	1.009(7)	1.004(6)
3.0	1.133(13)	1.044(12)	1.018(12)	1.010(12)
3.5	1.179(21)	1.057(19)	1.024(18)	1.014(18)
4.0	1.220(31)	1.070(27)	1.030(26)	1.018(26)
$\omega = 1.5$				
1.0	0.764(35)	0.939(43)	1.010(46)	1.032(47)
1.5	0.901(10)	0.968(11)	0.989(11)	0.994(11)
2.0	1	1	1	1
2.5	1.067(6)	1.017(6)	1.005(6)	1.003(6)
3.0	1.118(13)	1.030(12)	1.010(11)	1.006(11)
3.5	1.159(20)	1.039(18)	1.013(18)	1.008(18)
4.0	1.196(31)	1.049(27)	1.018(26)	1.012(26)
$\omega = 2.0$				
1.0	0.825(34)	1.014(42)	1.074(45)	1.078(45)
1.5	0.910(10)	0.978(11)	0.994(11)	0.995(11)
2.0	1	1	1	1
2.5	1.059(6)	1.010(5)	1.001(5)	1.000(5)
3.0	1.106(12)	1.019(11)	1.003(11)	1.002(11)
3.5	1.137(17)	1.020(15)	0.999(15)	0.998(15)
4.0	1.160(21)	1.018(18)	0.994(18)	0.993(18)

$\mu_0 = 2$ give trivially one, but we leave the results in order to guide the eyes. We give our results in Table XIV.

3. Study of the running in the nondegenerate ω case

Here we fix again both energy scales $(\mu_0, \mu) = (2.5 \text{ GeV}, 1.5 \text{ GeV})$, and we allow $\omega \neq \omega_0$. Our results are shown in Tables XV and XVI for $X = \gamma_\mu$ and in Tables XVII and XVIII for $X = \not{q}$.

TABLE XV. Running for the quark mass, γ_μ projector for $(\mu_0, \mu) = (2.5 \text{ GeV}, 1.5 \text{ GeV})$.

$(\mu_0,\mu)=(2.5,1.5)$ $\omega\downarrow$	σ_m	σ_m/LO	σ_m/NLO	$\sigma_m/NNLO$
$\boldsymbol{\omega_0 = 0.5}$				
0.5	1.229(27)	1.091(24)	1.035(23)	1.006(22)
1.0	1.308(29)	1.161(26)	1.067(23)	1.023(23)
1.5	1.373(30)	1.219(27)	1.094(24)	1.038(23)
2.0	1.425(32)	1.265(28)	1.113(25)	1.048(24)
2.5	1.473(34)	1.307(30)	1.131(26)	1.057(24)
3.0	1.515(35)	1.345(31)	1.145(27)	1.065(25)
3.5	1.551(36)	1.377(32)	1.156(27)	1.069(25)
4.0	1.568(33)	1.391(29)	1.154(24)	1.062(22)
$\boldsymbol{\omega_0 = 1.0}$				
0.5	1.103(18)	0.979(16)	0.969(16)	0.967(16)
1.0	1.174(18)	1.042(16)	0.999(16)	0.984(15)
1.5	1.232(19)	1.094(17)	1.024(16)	0.998(15)
2.0	1.279(20)	1.136(18)	1.042(16)	1.008(16)
2.5	1.322(21)	1.174(19)	1.059(17)	1.017(16)
3.0	1.360(22)	1.208(20)	1.073(18)	1.024(17)
3.5	1.392(22)	1.236(20)	1.083(17)	1.028(17)
4.0	1.407(22)	1.249(20)	1.080(17)	1.021(16)
$\boldsymbol{\omega_0 = 1.5}$				
0.5	1.059(17)	0.940(15)	0.961(15)	0.977(16)
1.0	1.128(16)	1.001(14)	0.992(14)	0.994(14)
1.5	1.184(17)	1.051(15)	1.016(15)	1.009(15)
2.0	1.229(18)	1.091(16)	1.035(15)	1.019(15)
2.5	1.271(19)	1.128(17)	1.051(16)	1.028(16)
3.0	1.307(20)	1.161(18)	1.065(17)	1.035(16)
3.5	1.338(20)	1.188(18)	1.075(16)	1.040(16)
4.0	1.353(13)	1.201(12)	1.073(10)	1.033(10)
$\boldsymbol{\omega_0 = 2.0}$				
0.5	1.002(15)	0.890(13)	0.934(14)	0.963(14)
1.0	1.067(14)	0.947(13)	0.964(13)	0.980(13)
1.5	1.119(15)	0.993(14)	0.987(13)	0.994(14)
2.0	1.162(16)	1.032(14)	1.005(14)	1.004(14)
2.5	1.201(17)	1.066(15)	1.021(14)	1.013(14)
3.0	1.236(18)	1.097(16)	1.034(15)	1.020(15)
3.5	1.265(18)	1.123(16)	1.044(15)	1.024(15)
4.0	1.279(12)	1.136(11)	1.043(10)	1.018(10)

TABLE XVI. Running for the quark mass, γ_μ projector for $(\mu_0, \mu) = (2.5 \text{ GeV}, 1.5 \text{ GeV})$ (continued).

$(\mu_0,\mu)=(2.5,1.5)$ $\omega\downarrow$	σ_m	σ_m/LO	σ_m/NLO	σ_m/NLO
$\boldsymbol{\omega_0 = 2.5}$				
0.5	0.952(12)	0.845(10)	0.907(11)	0.947(12)
1.0	1.013(11)	0.899(10)	0.937(10)	0.964(10)
1.5	1.064(12)	0.944(11)	0.960(11)	0.978(11)
2.0	1.105(13)	0.981(11)	0.978(11)	0.988(11)
2.5	1.143(14)	1.014(12)	0.994(12)	0.998(12)
3.0	1.176(15)	1.044(13)	1.007(13)	1.005(13)
3.5	1.203(14)	1.068(13)	1.016(12)	1.008(12)
4.0	1.217(9)	1.080(8)	1.015(8)	1.003(8)
$\boldsymbol{\omega_0 = 3.0}$				
0.5	0.911(11)	0.809(10)	0.887(10)	0.935(11)
1.0	0.970(10)	0.861(9)	0.915(9)	0.952(10)
1.5	1.018(11)	0.903(9)	0.938(10)	0.965(10)
2.0	1.057(11)	0.938(10)	0.955(10)	0.975(10)
2.5	1.092(12)	0.970(10)	0.970(10)	0.983(10)
3.0	1.124(12)	0.998(11)	0.982(11)	0.990(11)
3.5	1.150(12)	1.021(11)	0.992(11)	0.995(11)
4.0	1.163(7)	1.032(6)	0.990(6)	0.988(6)
$\boldsymbol{\omega_0 = 3.5}$				
0.5	0.879(10)	0.780(9)	0.872(10)	0.927(11)
1.0	0.935(9)	0.830(8)	0.899(9)	0.943(9)
1.5	0.982(9)	0.871(8)	0.922(9)	0.957(9)
2.0	1.019(10)	0.905(8)	0.938(9)	0.966(9)
2.5	1.054(10)	0.935(9)	0.953(9)	0.975(9)
3.0	1.084(11)	0.962(10)	0.965(10)	0.982(10)
3.5	1.110(11)	0.985(9)	0.975(9)	0.986(9)
4.0	1.122(5)	0.996(4)	0.973(4)	0.980(4)
$\boldsymbol{\omega_0 = 4.0}$				
0.5	0.846(10)	0.751(9)	0.853(10)	0.915(11)
1.0	0.901(9)	0.799(8)	0.880(9)	0.931(9)
1.5	0.945(9)	0.839(8)	0.902(9)	0.944(9)
2.0	0.982(10)	0.871(9)	0.918(9)	0.954(9)
2.5	1.014(10)	0.900(9)	0.932(9)	0.962(10)
3.0	1.044(11)	0.927(10)	0.945(10)	0.969(10)
3.5	1.068(10)	0.948(9)	0.954(9)	0.973(10)
4.0	1.080(5)	0.959(5)	0.952(5)	0.967(5)

TABLE XVII. Same as Table XVI for the $\displaystyle{\not}q$ projector. Again we have $(\mu_0, \mu) = (2.5 \text{ GeV}, 1.5 \text{ GeV})$.

$(\mu_0, \mu) = (2.5, 1.5)$

$\omega\downarrow$	σ_m	σ_m/LO	σ_m/NLO	$\sigma_m/NNLO$
$\boldsymbol{\omega_0 = 0.5}$				
0.5	1.194(23)	1.059(21)	1.012(20)	0.992(20)
1.0	1.294(26)	1.148(23)	1.052(21)	0.986(20)
1.5	1.378(29)	1.223(26)	1.085(23)	1.047(22)
2.0	1.447(33)	1.284(30)	1.109(26)	1.032(24)
2.5	1.513(38)	1.343(34)	1.133(29)	1.081(27)
3.0	1.574(42)	1.397(37)	1.155(30)	1.069(28)
3.5	1.631(41)	1.448(36)	1.175(29)	1.112(28)
4.0	1.661(40)	1.474(35)	1.177(28)	1.084(26)
$\boldsymbol{\omega_0 = 1.0}$				
0.5	1.050(17)	0.932(15)	0.943(15)	1.002(16)
1.0	1.138(18)	1.010(16)	0.980(16)	0.995(16)
1.5	1.212(20)	1.076(17)	1.010(16)	1.057(17)
2.0	1.274(22)	1.130(20)	1.033(18)	1.043(18)
2.5	1.332(26)	1.182(23)	1.056(21)	1.092(22)
3.0	1.386(29)	1.230(26)	1.076(22)	1.081(22)
3.5	1.436(28)	1.275(24)	1.095(21)	1.123(22)
4.0	1.461(33)	1.297(29)	1.096(24)	1.095(24)
$\boldsymbol{\omega_0 = 1.5}$				
0.5	0.985(11)	0.874(10)	0.924(10)	0.933(10)
1.0	1.068(10)	0.948(8)	0.960(9)	0.927(8)
1.5	1.138(13)	1.010(11)	0.991(11)	0.985(11)
2.0	1.196(16)	1.061(15)	1.013(14)	0.972(13)
2.5	1.250(21)	1.110(19)	1.035(17)	1.018(17)
3.0	1.301(24)	1.155(21)	1.055(19)	1.007(19)
3.5	1.348(21)	1.197(19)	1.074(17)	1.047(17)
4.0	1.372(19)	1.218(17)	1.075(15)	1.020(14)
$\boldsymbol{\omega_0 = 2.0}$				
0.5	0.921(9)	0.818(8)	0.896(9)	0.961(9)
1.0	0.998(9)	0.886(8)	0.930(8)	0.954(8)
1.5	1.064(10)	0.944(9)	0.960(9)	1.014(10)
2.0	1.117(13)	0.992(12)	0.981(12)	1.000(12)
2.5	1.168(17)	1.037(15)	1.002(15)	1.047(16)
3.0	1.216(20)	1.079(18)	1.022(17)	1.036(17)
3.5	1.260(18)	1.118(16)	1.040(15)	1.077(15)
4.0	1.283(19)	1.139(17)	1.041(16)	1.051(16)

TABLE XVIII. Running for the $\displaystyle{\not}q$ projector (continued).

$(\mu_0, \mu) = (2.5, 1.5)$

$\omega\downarrow$	σ_m	σ_m/LO	σ_m/NLO	$\sigma_m/NNLO$
$\boldsymbol{\omega_0 = 2.5}$				
0.5	0.862(7)	0.765(6)	0.864(7)	0.889(7)
1.0	0.935(7)	0.830(6)	0.899(7)	0.884(7)
1.5	0.997(8)	0.885(7)	0.927(7)	0.939(7)
2.0	1.048(10)	0.930(9)	0.949(9)	0.928(9)
2.5	1.096(13)	0.973(11)	0.970(11)	0.971(11)
3.0	1.141(15)	1.013(13)	0.989(13)	0.961(13)
3.5	1.181(12)	1.048(11)	1.005(11)	0.998(10)
4.0	1.203(21)	1.068(19)	1.007(18)	0.974(17)
$\boldsymbol{\omega_0 = 3.0}$				
0.5	0.818(6)	0.726(5)	0.842(6)	0.912(7)
1.0	0.887(7)	0.787(6)	0.875(7)	0.906(7)
1.5	0.945(7)	0.839(6)	0.903(6)	0.962(7)
2.0	0.993(8)	0.881(7)	0.923(8)	0.949(8)
2.5	1.038(11)	0.921(10)	0.943(10)	0.994(11)
3.0	1.080(13)	0.959(12)	0.962(12)	0.984(12)
3.5	1.119(11)	0.994(10)	0.978(10)	1.022(10)
4.0	1.139(20)	1.011(18)	0.979(17)	0.996(17)
$\boldsymbol{\omega_0 = 3.5}$				
0.5	0.780(6)	0.692(5)	0.822(6)	0.859(7)
1.0	0.845(6)	0.750(5)	0.855(6)	0.853(6)
1.5	0.901(6)	0.800(5)	0.882(6)	0.906(6)
2.0	0.947(8)	0.840(7)	0.902(7)	0.894(7)
2.5	0.990(11)	0.879(10)	0.921(10)	0.936(10)
3.0	1.030(13)	0.914(12)	0.939(12)	0.926(12)
3.5	1.068(11)	0.948(9)	0.956(10)	0.963(10)
4.0	1.086(17)	0.964(15)	0.957(15)	0.939(14)
$\boldsymbol{\omega_0 = 4.0}$				
0.5	0.741(8)	0.658(7)	0.799(9)	0.871(9)
1.0	0.804(8)	0.713(7)	0.830(8)	0.865(8)
1.5	0.856(9)	0.760(8)	0.856(9)	0.919(10)
2.0	0.900(12)	0.799(10)	0.876(11)	0.907(12)
2.5	0.941(15)	0.835(13)	0.894(14)	0.949(15)
3.0	0.979(17)	0.869(15)	0.912(16)	0.940(16)
3.5	1.014(15)	0.900(13)	0.928(13)	0.977(14)
4.0	1.033(12)	0.917(10)	0.929(10)	0.952(11)

APPENDIX F: CONTINUUM EXTRAPOLATION

As an example of continuum extrapolations, we show $\Sigma_m^{(\gamma_\mu)}(\mu, \mu_0, \omega, \omega_0)$ in Figs. 24 and 25. The magenta error bar is a systematic error, obtained by adding half the difference between the extrapolated value, $\sigma_m^{(\gamma_\mu)}(\mu, \mu_0, \omega, \omega_0)$, and the value obtained on the finest lattice.
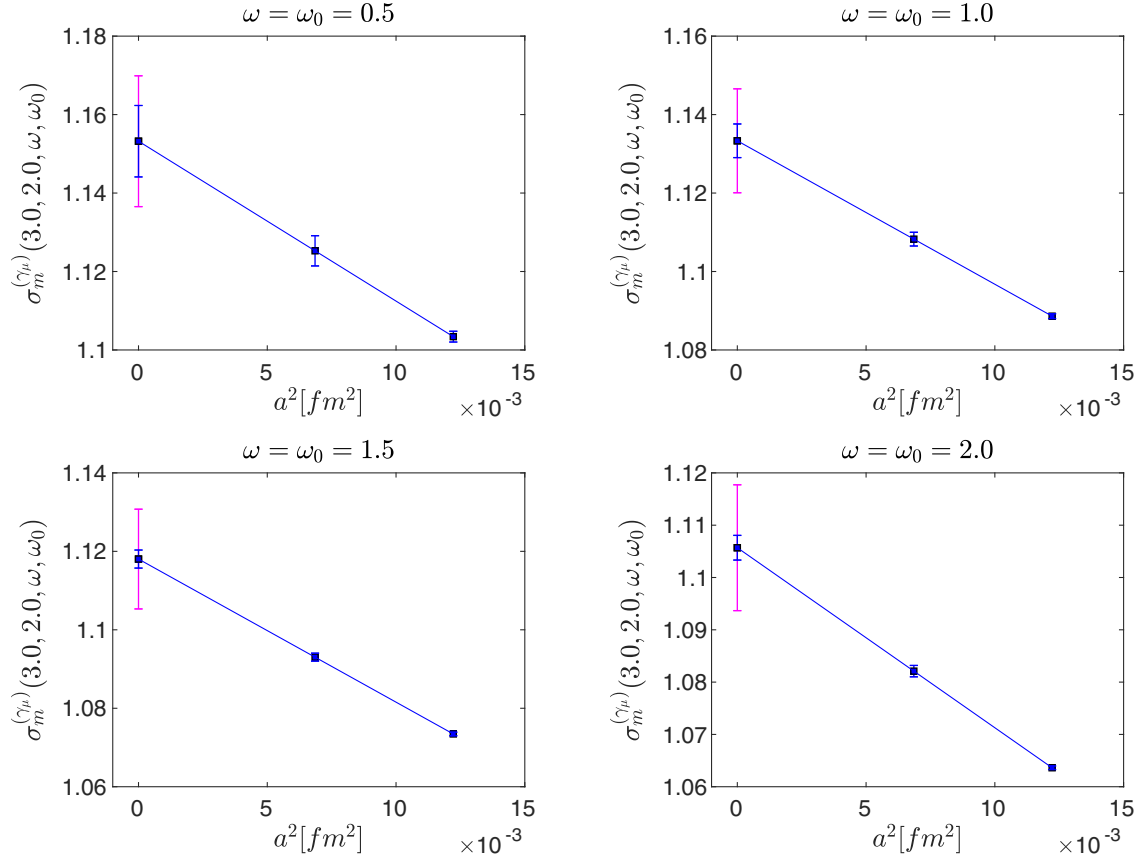

FIG. 24. Continuum extrapolations for Σ_m. We choose $(X, \mu, \mu_0) = (\gamma_\mu, 2\text{ GeV}, 3\text{ GeV})$ and show our results for the different values of $\omega = \omega_0$ from 0.5 (top left corner) to 2.0 (bottom right corner). We included an estimation of the error due to the continuum extrapolation (error bar in magenta, see text).
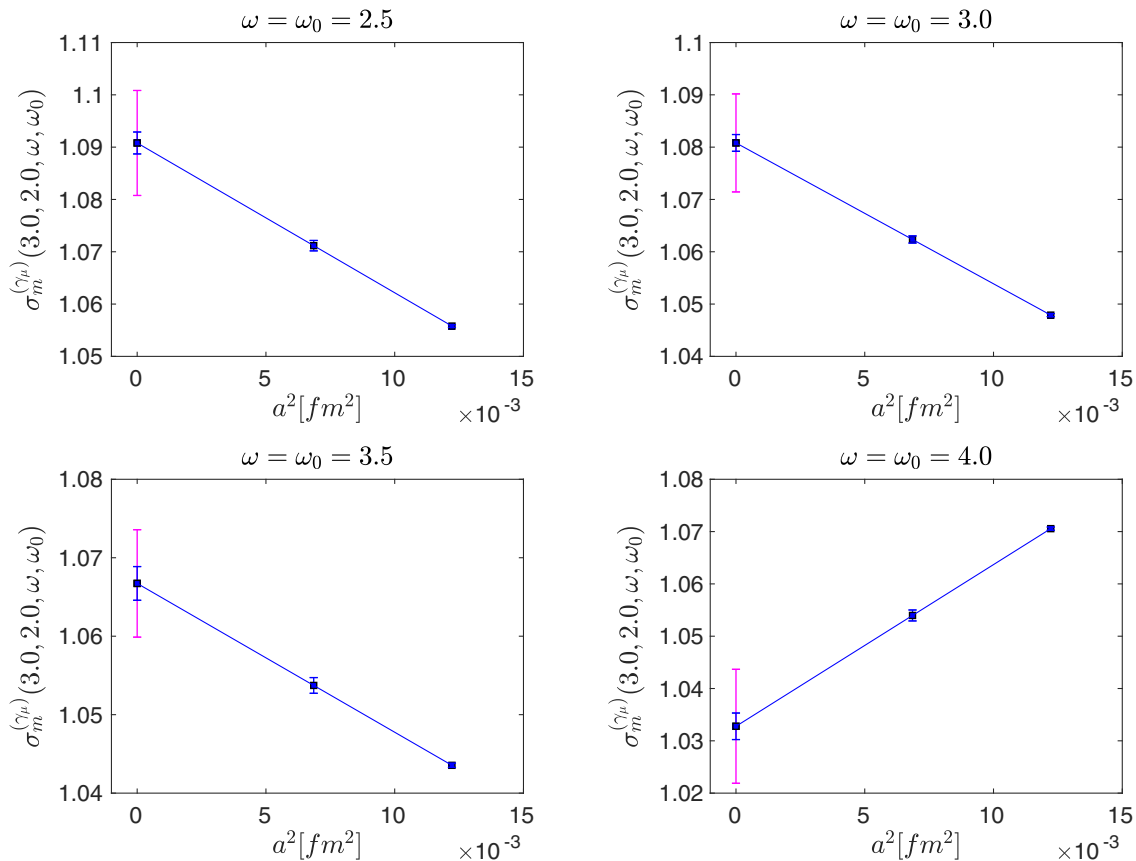
FIG. 25. Same as Fig. 24 for $\omega = \omega_0 = 2.5, 3.0, \ldots, 4.0$.

[1] M. Lüscher, R. Narayanan, P. Weisz, and U. Wolff, The Schrödinger functional: A renormalizable probe for non-Abelian gauge theories, Nucl. Phys. **B384**, 168 (1992).

[2] S. Sint, On the Schrödinger functional in QCD, Nucl. Phys. **B421**, 135 (1994).

[3] G. Martinelli, C. Pittori, C. T. Sachrajda, M. Testa, and A. Vladikas, A general method for nonperturbative renormalization of lattice operators, Nucl. Phys. **B445**, 81 (1995).

[4] P. Boyle, L. Del Debbio, and A. Khamseh, Massive momentum-subtraction scheme, Phys. Rev. D **95**, 054505 (2017).

[5] E. Franco and V. Lubicz, Quark mass renormalization in the MS and RI schemes up to the NNLO order, Nucl. Phys. **B531**, 641 (1998).

[6] Y. Aoki et al., Nonperturbative renormalization of quark bilinear operators and B(K) using domain wall fermions, Phys. Rev. D **78**, 054510 (2008).

[7] N. Garron, R. J. Hudspith, and A. T. Lytle (RBC/UKQCD Collaborations), Neutral kaon mixing beyond the standard model with $n_f = 2 + 1$ chiral fermions part 1: Bare matrix elements and physical results, J. High Energy Phys. 11 (2016) 001.

[8] P. A. Boyle, N. Garron, R. J. Hudspith, C. Lehner, and A. T. Lytle (RBC, UKQCD Collaborations), Neutral kaon mixing beyond the standard model with $n_f = 2 + 1$ chiral fermions. Part 2: Nonperturbative renormalization of the $\Delta F = 2$ four-quark operators, J. High Energy Phys. 10 (2017) 054.

[9] C. Sturm, Y. Aoki, N. H. Christ, T. Izubuchi, C. T. C. Sachrajda, and A. Soni, Renormalization of quark bilinear operators in a momentum-subtraction scheme with a non-exceptional subtraction point, Phys. Rev. D **80**, 014501 (2009).

[10] M. Gorbahn and S. Jager, Precise $\overline{\text{MS}}$ light-quark masses from lattice QCD in the regularization invariant symmetric momentum-subtraction scheme, Phys. Rev. D **82**, 114001 (2010).

[11] L. G. Almeida and C. Sturm, Two-loop matching factors for light quark masses and three-loop mass anomalous dimensions in the regularization invariant symmetric momentum-subtraction schemes, Phys. Rev. D **82**, 054017 (2010).

[12] J. Gracey, RI′/SMOM scheme amplitudes for quark currents at two loops, Eur. Phys. J. C **71**, 1567 (2011).

[13] A. Bednyakov and A. Pikelner, Quark masses: N3LO bridge from RI/SMOM to $\overline{\text{MS}}$ scheme, Phys. Rev. D **101**, 091501 (2020).

[14] B. A. Kniehl and O. L. Veretin, Bilinear quark operators in the RI/SMOM scheme at three loops, Phys. Lett. B **804**, 135398 (2020).

[15] R. Arthur and P. Boyle (RBC, UKQCD Collaborations), Step scaling with off-shell renormalization, Phys. Rev. D **83**, 114511 (2011).

[16] Y. Aoki et al. (RBC, UKQCD Collaborations), Continuum limit physics from $2 + 1$ flavor domain wall QCD, Phys. Rev. D **83**, 074508 (2011).

[17] Y. Aoki et al., Continuum limit of B_K from $2 + 1$ flavor domain wall QCD, Phys. Rev. D **84**, 014503 (2011).

[18] Y. Bi, H. Cai, Y. Chen, M. Gong, K.-F. Liu, Z. Liu, and Y.-B. Yang, RI/MOM and RI/SMOM renormalization of overlap quark bilinears on domain wall fermion configurations, Phys. Rev. D **97**, 094501 (2018).

[19] C. Chang et al., A per-cent-level determination of the nucleon axial coupling from quantum chromodynamics, Nature (London) **558**, 91 (2018).

[20] J. M. Bell and J. A. Gracey, Bilinear quark operator renormalization at generalized symmetric point, Phys. Rev. D **93**, 065031 (2016).

[21] J. A. Gracey and R. M. Simms, Renormalization of QCD in the interpolating momentum subtraction scheme at three loops, Phys. Rev. D **97**, 085016 (2018).

[22] M. Göckeler, R. Horsley, H. Oelrich, H. Perlt, D. Petters, P. E. L. Rakow, A. Schäfer, G. Schierholz, and A. Schiller, Nonperturbative renormalization of composite operators in lattice QCD, Nucl. Phys. **B544**, 699 (1999).

[23] K. Chetyrkin and A. Retey, Renormalization and running of quark mass and field in the regularization invariant and MS schemes at three loops and four loops, Nucl. Phys. **B583**, 3 (2000).

[24] Y. Aoki et al., FLAG review 2021, Eur. Phys. J. C **82**, 869 (2022).

[25] P. Baikov, K. Chetyrkin, and J. Kühn, Five-Loop Running of the QCD Coupling Constant, Phys. Rev. Lett. **118**, 082002 (2017).

[26] F. Herzog, B. Ruijl, T. Ueda, J. Vermaseren, and A. Vogt, The five-loop beta function of Yang-Mills theory with fermions, J. High Energy Phys. 02 (2017) 090.

[27] T. Luthe, A. Maier, P. Marquard, and Y. Schroder, The five-loop beta function for a general gauge group and anomalous dimensions beyond Feynman gauge, J. High Energy Phys. 10 (2017) 166.

[28] P. Zyla et al. (Particle Data Group Collaboration), Review of particle physics, Prog. Theor. Exp. Phys. **2020**, 083C01 (2020).

[29] K. Chetyrkin, J. H. Kühn, and M. Steinhauser, RunDec: A mathematica package for running and decoupling of the strong coupling and quark masses, Comput. Phys. Commun. **133**, 43 (2000).

[30] Y. Shamir, Chiral fermions from lattice boundaries, Nucl. Phys. **B406**, 90 (1993).